Mitochondrial perturbation of the epithelium causes microbial dysbiosis and unresolved tissue injury in intestinal inflammation

Authors

Elisabeth Urbauer[1]*, Doriane Aguanno[1]*, Nora Mindermann[1], Hélène Omer[1], Amira Metwaly[1], Sevana Khaloian[1], Sandra Reitmeier[1], Marianne Remke[2], Sebastian Jarosch[3], Samuel Huber[4], Dirk H. Busch[3], Bärbel Stecher[5,6], Matthieu Allez[7], Katja Steiger[2], Eva Rath[1], Dirk Haller[1,8]

Authors' affiliation

[1] Chair of Nutrition and Immunology, Technische Universität München, Freising-Weihenstephan, Germany

[2] Institute of Pathology, Technische Universität München, Munich, Germany

[3] Institute for Medical Microbiology, Immunology and Hygiene, Technische Universität München, Munich, Germany

[4] Section of Molecular Immunology and Gastroenterology, I. Department of Medicine, University Medical Center Hamburg-Eppendorf, Hamburg, Germany

[5] Max von Pettenkofer-Institute for Hygiene and Clinical Microbiology, Ludwig-Maximilians University of Munich, Munich, Germany

[6] German Center for Infection Research, Partner site LMU Munich, Munich, Germany

[7] Department of Gastroenterology, Hôpital Saint Louis, APHP, INSERM UMRS 1160, Paris Diderot, Sorbonne Paris-Cité University, Paris, France

[8] ZIEL Institute for Food and Health, Technische Universität München, Freising, Germany dirk.haller@tum.de

*These authors contributed equally to this project.

Abstract

Mitochondrial dysfunction in intestinal epithelial cells (IECs) is associated with chronic inflammation. To understand how microbial-metabolic circuits contribute to tissue injury, we disrupt mitochondrial function in IECs by deleting heat shock protein 60 (Hsp60$^{\Delta/\Delta IEC}$). While metabolic perturbation causes self-resolving tissue injury, inflammation is accelerated in the susceptible host (Hsp60$^{\Delta/\Delta IEC}$;*Il10*$^{-/-}$). Interestingly, metabolic injury induces microbial dysbiosis, including *Bacteroides* spp. expansion. Tissue pathology is absent in the distal colon of germfree (GF) Hsp60$^{\Delta/\Delta IEC}$ mice, highlighting bacterial control of metabolic injury. In line, host tryptophan metabolism is rewired, and the absence of bacterial-mediated AhR signaling (Hsp60$^{\Delta/\Delta IEC}$;*AhR*$^{-/-}$) causes severe acceleration of injury independent of IL-22. Furthermore, selective colonization of GF Hsp60$^{\Delta/\Delta IEC}$ mice with OMM^{12} induces metabolic injury and *Bacteroides caecimuris* expansion, which generates metabolic injury in mono-colonized mice. In conclusion, mitochondrial perturbation of the epithelium causes dysbiotic expansion of *Bacteroides* spp., supporting the concept that microbe-host cross-talk contributes to metabolic injury in intestinal inflammation.

Keywords: metabolic injury, mitochondrial dysfunction, inflammation, IBD, microbiome, Bacteroides

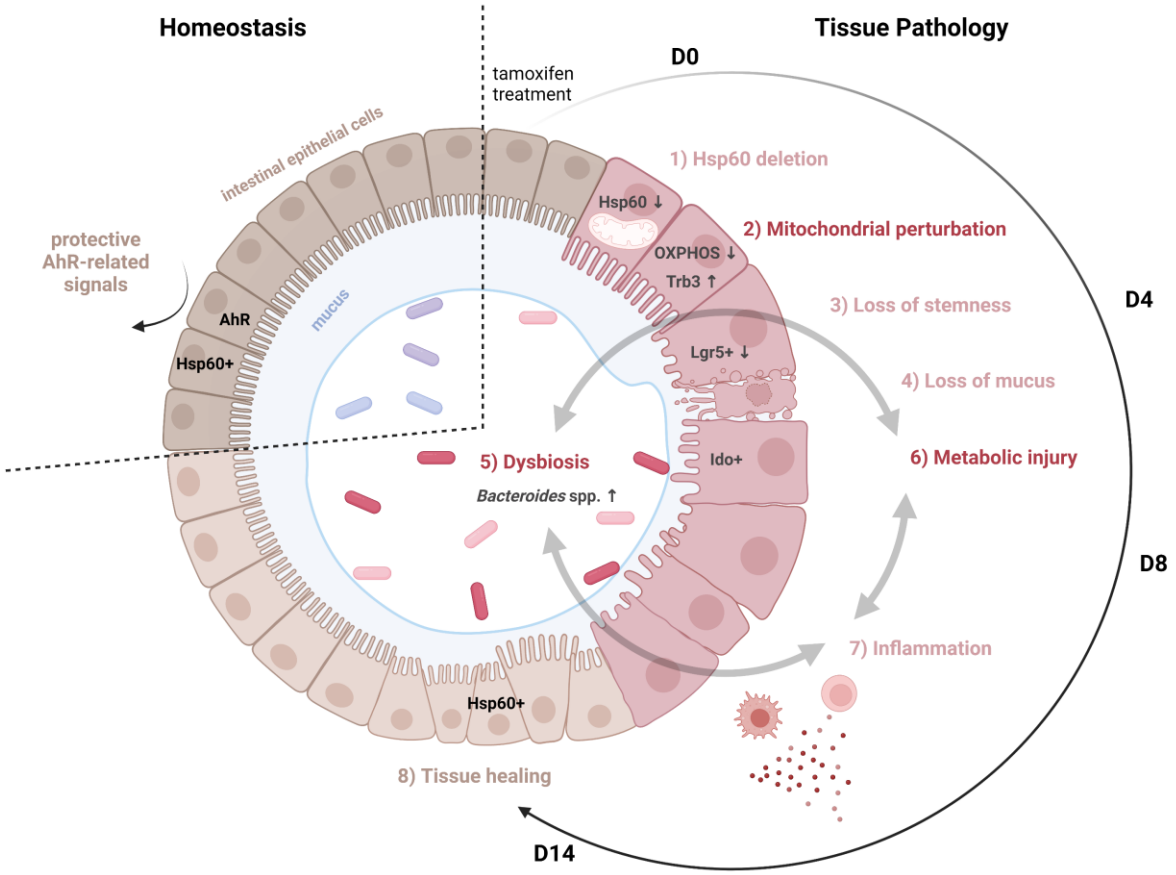

Graphical Abstract: Control of metabolic injury by microbial signals.

- Hsp60 deletion is induced in intestinal epithelial cells leading to mitochondrial perturbation, causing a shift in colonocyte metabolism (1, 2)
- Intestinal crypts display loss of stemness and weakening of the mucus barrier accompanied by dysbiotic changes, notably expansion of *Bacteroides* spp. (3 – 6)
- The injury phenotype is accompanied by immune cell recruitment and loss of regulatory mechanisms in a colitis-susceptible model (7)
- AhR-dependent signals are critical to maintain balanced bacterial-metabolic circuits for tissue healing and homeostasis (8)

Created with BioRender.com.

D: day; Hsp60+: heat shock protein 60-positive; Lgr5+: leucine-rich repeat-containing G-protein coupled receptor 5-positive; AhR: aryl hydrocarbon receptor; OXPHOS: oxidative phosphorylation; MT-UPR: mitochondrial unfolded protein response; Trb3: tribbles pseudokinase 3; Ido1: indoleamine 2, 3-dioxygenase 1.

Introduction

The intestinal epithelium is exposed to a diverse and complex microbial milieu at the mucosal interface. A breach in epithelial barrier integrity is associated with inflammatory pathologies[1] and necessitates a fine-tuned balance of epithelial renewal for healing processes. In particular, the high energy demand of the inflamed mucosa requires mitochondria as central coordinators of metabolic circuits between the host and microbiome, adding a new aspect to the "energy deficiency" hypothesis[2]. Mitochondria control intestinal epithelial cell (IEC) metabolism, including oxidative phosphorylation (OXPHOS), and influence IEC fate and properties[3]. A cornerstone in this homeostatic regulation is the mitochondrial unfolded protein response (MT-UPR), a conserved signaling pathway triggered upon protein aggregation or misfolding in the mitochondrial matrix[4]. While this autoregulatory mechanism aims to restore homeostasis during acute stress by controlling epithelial self-renewal[3], its sustained activation is associated with disease pathogenesis[5,6].

Microbiome-host mutualism is required for intestinal homeostasis, and its disruption contributes to the initiation and progression of diseases[7], including inflammatory bowel diseases (IBD)[8], graft-versus-host disease (GvHD)[9], and type 2 diabetes[10]. Among the > 240 identified IBD genetic risk loci, genes associated with mitochondrial function point towards its implication in IBD[11,12]. In line, we showed that conditional deletion of the heat shock protein 60 (Hsp60) in the murine small intestine induces mitochondrial impairment leading to a loss of stemness and epithelial injury[13]. Accordingly, we demonstrated that activated MT-UPR signaling is linked to IBD-related inflammation in patients[14]. While loss of the mitochondrial protein prohibitin 1 triggers mitochondrial impairment in Paneth cells and subsequent ileitis in mice[15], mitochondrial dysfunction in the ISC niche predicts disease recurrence in Crohn's disease patients[16]. Even though the involvement of the microbiome in IBD has been extensively studied, data on the link between mitochondrial dysfunction and microbial composition is scarce. An intriguing new concept suggests that metabolic reprogramming of IECs contributes to microbial dysbiosis[17], highlighting the bi-directional cross-talk of the microbiome and host. Mitochondria detect diet- and microbiome-derived metabolites, which modulate the ISC niche and IEC functions. Moreover, they participate in sensing host- and microbial-derived signals, notably through Toll-Like Receptor signaling pathways[18] as well as tryptophan metabolites and Arylhydrocarbon receptor (AhR) signaling pathways[19]. We hypothesize that failure of mitochondrial function at the intestinal interface and disruption of microbial-metabolic circuits contribute to dysbiosis and chronic intestinal inflammation.

To investigate microbe-host cross-talks and their contribution to metabolic injury as a novel hypothesis for recurrent intestinal inflammation, we induce mitochondrial dysfunction by deleting Hsp60 specifically in murine IECs. We show that mitochondrial impairment causes metabolic injury, a self-autonomous mechanism of tissue wounding in response to

mitochondrial perturbation, which accelerates the onset of colitis and is associated with microbial dysbiosis. Remarkably, *Bacteroides caecimuris* temporally and spatially control metabolic injury. On a cellular level, host tryptophan metabolism is rewired, and bacterial-dependent AhR activation is essential for survival. Conclusively, these data indicate that mitochondria are a cornerstone in regulating cellular metabolism and function, and microbial-metabolic circuits control intestinal tissue homeostasis.

Results

Metabolic injury accelerates the onset of inflammation

Mitochondrial function regulates stem cell homeostasis, and disruption of metabolic circuits in the intestinal epithelium is an emerging mechanism in the development of recurrent inflammation. To address the functional consequences of mitochondrial dysfunction in IECs, we deleted *Hsp60* (Hsp60$^{\Delta/\Delta IEC}$) in mice housed under specific pathogen-free (SPF) conditions, causing transient weight loss (Fig.1a,b). Hsp60-deficient organoids demonstrated reduced proliferation and ATP production, as well as activated MT-UPR signaling (*Trb3*) and reduced stemness (*Lgr5*) (Extended Data Fig.1a-e). In line, colonic gene expression analysis confirmed the *Hsp60* deletion and activation of MT-UPR signaling (*Trb3*) in mice (Extended Data Fig.2a,b), demonstrating that *Hsp60* deletion induces MT-UPR signaling *in vivo* and *ex vivo*. In addition, microarray analysis of Hsp60-deficient colonocytes confirmed MT-UPR induction and highlighted that mitochondrial dysfunction is associated with metabolic reprogramming (reduction in OXPHOS, increase in glycolysis) (Extended Data Fig.1f,g).

Interestingly, colonic histopathological evaluation revealed an aberrant epithelial architecture, which was characterized by the resorption of damaged crypts (dilated and attenuated crypts filled with cellular debris) and compensatory hyperproliferation of cells that regained Hsp60. This metabolic injury phenotype was followed by regenerative responses leading to tissue restitution (Fig.1c). A new score for epithelial aberration (Fig.1d) and measurement of crypt depth (Extended Data Fig.2c) highlighted that metabolic disruption of the colonic epithelium causes self-resolving tissue injury. Immunohistochemistry staining and quantification of Hsp60 confirmed the loss and regain of Hsp60, the latter presumably originating from stem cells escaping Hsp60 deletion[13] (Fig.1e; Extended Data Fig.2d). Highly proliferative tissue regions (Ki67+) were characterized by strong expression of Hsp60, and *vice versa*, Hsp60 deficiency abrogated Ki67 expression indicating reduced crypt proliferation (Fig.1f).

Additionally, metabolic injury was accompanied by elevated levels of the pro-inflammatory cytokine *Tnf* and an increase in Ly6G+ cells and CD8+ T-cells (Extended Data Fig.2e-g). To further investigate the impact of metabolic injury on the onset of inflammation, we crossed Hsp60$^{\Delta/\Delta IEC}$ with Interleukin (IL)-10 knockout mice (Hsp60$^{\Delta/\Delta IEC}$;*Il10*$^{-/-}$; Fig.1g). Analysis of later time points was not feasible since mice depicted reduced survival and reached termination criteria due to weight loss and changes in stool consistency (Extended Data Fig.2h). In contrast to Hsp60$^{\Delta/\Delta IEC}$;*Il10*$^{+/+}$ mice, Hsp60$^{\Delta/\Delta IEC}$;*Il10*$^{-/-}$ mice did not recover from weight loss (Fig.1h). Of note, IL-10 deficiency did not impact genetically-driven activation of *Trb3* (Fig.1i). Most remarkably, at day 14, two out of six Hsp60$^{\Delta/\Delta IEC}$;*Il10*$^{-/-}$ mice displayed an accelerated inflammatory phenotype in the distal colon, which was corroborated by an elevated tissue pathology index, elongated crypts, and an increase in aberrant epithelial architecture

(Fig.1j,l,m; Extended Data Fig.2i), suggesting a disrupted regenerative response to metabolic injury in the absence of IL-10. Of note, the regain of Hsp60 was independent of IL-10 (Fig.1k). In line with tissue inflammation, gene expression of *Tnf* and serum protein levels of serum amyloid A (Saa) were increased (Extended Data Fig.2j,k). Since Hsp60$^{fl/fl}$;*Il10*$^{-/-}$ mice did not develop colitis at such an early time point, this data provides further evidence that metabolic injury triggers the onset or recurrence of chronic inflammation.

Metabolic injury drives dysbiotic changes in the intestinal microbiota

Since microbial dysbiosis is a cornerstone in IBD pathogenesis, we analyzed the intestinal microbiome in the course of metabolic injury. 16S rRNA amplicon sequencing of colonic content revealed that metabolic injury was associated with rapid but transient changes in microbiota composition, including a drop in species richness and Shannon effective (α-diversity) (Fig.2a), as well as changes in the community profile (β-diversity) (Fig.2b). Analysis of differentially abundant taxa revealed six significantly altered genera, including *Bacteroides* spp. (Fig.2c). Interestingly, *Bacteroides* spp. showed the highest overall abundance and were transiently increased during metabolic injury. Shallow shotgun metagenomics revealed the presence of *B. caecimuris, B. uniformis,* and *Phocaeicola vulgatus* (Fig.2d). Their enrichment following mitochondrial dysfunction suggests that intestinal dysbiosis precedes metabolic injury. Since mucus-filled goblet cells (GCs) are essential for microbiome-host cross-talk, we further investigated their involvement in injury processes. Indeed, loss of GCs precedes tissue injury (Extended Data Fig.3a,b), providing a hallmark for disease onset.

While these changes were transient in Hsp60$^{\Delta/\Delta IEC}$ mice, alterations in α- and β-diversity were more pronounced at day 8 (Extended Data Fig.3c-e) and persisted at day 14 in Hsp60$^{\Delta/\Delta IEC}$;*Il10*$^{-/-}$ mice (Fig.2e,f). In line, the increased relative abundance of *Bacteroides* spp. persisted in Hsp60$^{\Delta/\Delta IEC}$;*Il10*$^{-/-}$ mice (Fig.2g), illustrating the rapid adaption of the microbiome to disturbances in IEC metabolism or signaling. In parallel and indicative of a disrupted regenerative response, Hsp60$^{\Delta/\Delta IEC}$;*Il10*$^{-/-}$ mice showed a persistent reduction in GCs (Fig.2h,i). In addition, bacterial profiling of fecal samples from 468 IBD patients[20,21] showed an increased relative abundance of *Bacteroides* spp. associated with intestinal inflammation (Extended Data Fig.3f,g).

Bacterial control of metabolic injury

To address the question whether bacterial changes are the cause or consequence of metabolic injury, we generated germfree (GF) Hsp60$^{\Delta/\Delta IEC}$ mice (Fig.3a). Compared to SPF housing, weight reduction was mild (Fig.3b) despite activated MT-UPR signaling (*Trb3*) (Fig.3c), and the kinetic of Hsp60 regain in the crypt epithelium was similar in the presence or absence of bacteria (Fig.3d,e; Extended Data Fig.4a). Most striking, histopathological evaluation revealed the absence of metabolic injury and inflammation in the middle and distal colon (Fig.3f-h),

supporting the hypothesis that bacteria are involved in regulating metabolic injury. The ileum and proximal colon largely retained the formation of an aberrant epithelial architecture (Fig.3g; Extended Data Fig.4b-d), suggesting that cell-autonomous mechanisms drive the injury phenotype in these tissue segments. Contrary to SPF housing, stemness and mucus barrier were not impaired in the absence of bacteria (Extended Data Fig.4e-g). Similar to Hsp60-deficient mice, the induction of mitochondrial dysfunction in the epithelium of GF Hsp60$^{\Delta/\Delta IEC}$;*Il10*$^{-/-}$ mice did not cause severe weight loss and reduced survival (Fig.3i,j) despite the increased disease susceptibility. Importantly, histopathological evaluation revealed the absence of metabolic injury and inflammation in the distal colon of GF Hsp60$^{\Delta/\Delta IEC}$;*Il10*$^{-/-}$ mice (Fig.3k-m), supporting the pivotal role of bacteria in regulating metabolic injury and the recurrence or onset of inflammation.

Host tryptophan metabolism is rewired during metabolic injury

To assess molecular changes during metabolic injury, we performed RNA NanoString® analysis of colonic tissue from SPF and GF Hsp60$^{\Delta/\Delta IEC}$ mice targeting ~ 800 metabolic genes. At day 0, 45 genes showed a fold change greater than ± 2 under SPF conditions, out of which 10 were mitochondria-related (Fig.4a). Patterns reflecting cellular changes were still present but already attenuated on day 8. In contrast, only 10 genes showed a fold change greater than ± 2 at day 0 under GF conditions (Fig.4b), indicating that changes in cellular metabolism are dependent on bacterial signals. KEGG pathway analysis of the 45 regulated genes under SPF conditions identified tryptophan metabolism as the most enriched pathway (Fig.4c). Indoleamine 2,3-dioxygenase 1 (Ido1) is the key enzyme involved in the host-related tryptophan-degrading kynurenine pathway, being upregulated under SPF conditions at both time points. Immunofluorescence analysis confirmed transiently increased Ido1 expression during metabolic injury in the crypts of SPF-housed Hsp60$^{\Delta/\Delta IEC}$ mice and persistent expression in Hsp60$^{\Delta/\Delta IEC}$;*Il10*$^{-/-}$ mice (Fig.4d upper and lower panel). On the contrary, Ido1 expression was completely absent under GF conditions (Fig.4d middle panel), highlighting the importance of microbial signals in rewiring host tryptophan metabolism.

To identify factors inducing Ido1, we treated Hsp60-deficient organoids with the inflammation-associated cytokines Tnf and Ifnγ as well as lipopolysaccharides (LPS) and cecal water from Hsp60$^{\Delta/\Delta IEC}$ mice (Fig.4e). Strikingly, *Ido1* expression was elevated in response to inflammatory cytokines, while none of the luminal factors induced its expression (Fig.4f). To elucidate the impact of increased Ido1 levels, we treated Hsp60-deficient organoids with the Ido1 downstream metabolite 3-hydroxyanthranilic acid (3-HAA) as well as the Ido1 antagonist dimethyltryptamine (1-D-MT). Interestingly, 3-HAA reduced stemness (*Lgr5*) in both control and knockout organoids but selectively enhanced MT-UPR signaling (*Trb3*) in the absence of Hsp60 (Fig.4g). Concomitant to these findings, 3-HAA reduced the survival and ATP

production of Hsp60-deficient organoids isolated after *Hsp60*-deletion *in vivo* (Extended Fig.5). In conclusion, these data suggest that upon mitochondrial perturbation in IECs, host-derived kynurenines detrimentally contribute to tissue injury.

Ahr signaling is a protective mechanism against metabolic injury

Given the importance of tryptophan metabolism, we assessed the involvement of host-sensing mechanisms in modulating injury and regenerative processes targeting the environmental sensor AhR (Hsp60$^{\Delta/\Delta IEC}$;*AhR*$^{-/-}$ mice; Fig.5a). Unexpectedly, SPF-housed Hsp60$^{\Delta/\Delta IEC}$;*AhR*$^{-/-}$ mice displayed a dramatically reduced survival (Fig. 5b). Most animals reached termination criteria between day 0 and 2, notably due to weight loss (Extended Data Fig.6a) and diarrhea. Histopathological evaluation at day 0 showed a severe loss of epithelial architecture in the ileum of these mice (Extended Data Fig.6b,c), suggesting an accelerated metabolic injury onset leading to death in the absence of AhR.

Remarkably, antibiotics abrogated the lethal phenotype of Hsp60$^{\Delta/\Delta IEC}$;*AhR*$^{-/-}$ mice (Fig.5a,b; Extended Data Fig.6a). Colonic tissue injury was retained at day 8 and persisted until day 14 (Fig.5c,d). Similar to GF Hsp60$^{\Delta/\Delta IEC}$ mice, tissue injury was absent in the distal but not the proximal colon of Hsp60$^{\Delta/\Delta IEC}$;*AhR*$^{+/+}$ mice (Fig.5d; Extended Data Fig.6d). Consistent with the importance of bacterial signals in regulating colonic injury, antibiotic exposure led to a 2-fold reduction of bacterial mass (Extended Data Fig.6e), massively decreased α-diversity, and complete depletion of *Bacteroides* spp. in feces (Fig.5e,f). Hsp60$^{\Delta/\Delta IEC}$;*AhR*$^{+/+}$ mice showed a high relative abundance of *Bacteroides* spp. compared to Hsp60$^{fl/fl}$;*AhR*$^{-/-}$ littermates (Fig.5f), confirming the selective enrichment under Hsp60 deficiency. Hsp60$^{\Delta/\Delta IEC}$;*AhR*$^{+/+}$ mice presented increased levels of inflammation in the distal and proximal colon at day 14 (Extended Data Fig.6f,g). Of note and despite decreased α-diversity, the abundance of *Bacteroides* ssp. was retained in Hsp60$^{\Delta/\Delta IEC}$;*AhR*$^{-/-}$ mice not receiving antibiotics (water control; Fig.5f), supporting the hypothesis that the reduction in bacterial load or depletion of *Bacteroides* spp. prevents metabolic injury and intestinal failure.

To further elucidate the protective role of AhR, we focused on the IL-22 pathway, a major downstream signaling pathway of AhR. Since IL-22 was increased in colonic tissue during metabolic injury (Extended Data Fig.6h), we generated Hsp60$^{\Delta/\Delta IEC}$;*Il22ra1*$^{-/-}$ mice (Fig.5g). Interestingly, absence of the IL-22 receptor did not affect weight development during metabolic injury (Fig.5h). In line, histological evaluation demonstrated no difference in epithelial aberration with or without IL-22 signaling (Fig.5i,j), indicating that this tissue cytokine is not involved in modulating injury and regeneration.

Bacteroides caecimuris induces metabolic injury

Considering the importance of bacteria in controlling injury of the distal colon, we addressed whether the Oligo-Mouse-Microbiota (OMM^{12}) synthetic bacterial community[22,23], initiates metabolic injury. The colonization of GF $Hsp60^{\Delta/\Delta IEC}$ mice with OMM^{12} (Fig.6a) regulated *Hsp60* and *Trb3* gene expression similar to SPF conditions (Fig.6b,c). Importantly, histopathological analysis showed metabolic injury in the distal colon, including the presence of Hsp60-positive hyperproliferative as well as Hsp60-negative damaged crypts (Fig.6d; Extended Data Fig.7a). Epithelial aberration, inflammation, and crypt depth were elevated (Fig.6e,f; Extended Data Fig.7b), providing proof-of-concept that simplified bacterial communities are sufficient to induce metabolic injury in the distal colon.

The quantification of bacterial abundances of all 12 strains using 16S targeted qPCR showed that *Bacteroides caecimuris* was elevated from day 4 (Fig.6g), supporting our previous data showing an increase of *Bacteroides* spp. preceding metabolic injury. In addition, the abundance of *Akkermansia muciniphila* and *Turicimonas muris* was elevated. All other bacterial species did not show changes in abundances (Extended Data Fig.8a).

To further dissect the contribution of *B. caecimuris* to metabolic injury, we mono-colonized GF $Hsp60^{\Delta/\Delta IEC}$ mice (Fig.6a). Altered gene expression levels of *Hsp60* and *Trb3* confirmed the experimental setup (Extended Data Fig.7c,d). Strikingly, *B. caecimuris* alone was sufficient to induce metabolic injury in the distal colon. Histological evaluation revealed the presence of hyperproliferative and damaged crypts (Fig.6h), as well as an increase in epithelial aberration and tissue inflammation (Fig.6i,j).

Since the abundance of *A. muciniphila* was elevated during OMM^{12}-induced metabolic injury, we performed a dual-colonization with *B. caecimuris* and *A. muciniphila* (Fig.6a). Interestingly, the presence of *A. muciniphila* reduced the abundance of *B. caecimuris* (Fig.6k) and completely prevented the induction of metabolic injury (Fig.6h-j). Notably, bacterial abundance of *B. caecimuris* and *A. muciniphila* was similar in both genotypes (Fig.6k; Extended Data Fig.8b).

To test whether *B. caecimuris*-induced metabolic injury is specific, we further colonized GF $Hsp60^{\Delta/\Delta IEC}$ mice with *L. reuteri* (Fig.6a), a bacterium with unchanged abundance during OMM^{12}-induced metabolic injury (Extended Data Fig.8a). Bacterial abundance did not differ between genotypes (Extended Data Fig.8c), and *B. caecimuris* alone or in combination with *A. muciniphila* colonized the colon with 10^{11} CFUs, whereas *L. reuteri* reached only 10^{9} CFUs. Importantly, *L. reuteri* could not induce metabolic injury in the distal colon (Fig.6h-j), highlighting the specificity of *B. caecimuris*.

Discussion

Mitochondria are a cornerstone in the control of cellular metabolism and function[6]. We previously demonstrated that conditional deletion of Hsp60 in the small intestinal epithelium initiates stem cell loss and crypt absorption, providing proof-of-concept that mitochondrial perturbation contributes to tissue injury[13]. In the present study, we identify microbial-metabolic circuits as the underlying cause of colonic tissue injury, suggesting a novel mechanism for recurrent inflammation. Consistently, the resolution of metabolic injury is disrupted in Hsp60$^{\Delta/\Delta IEC}$ mice in the absence of IL-10, leading to delayed crypt regeneration and accelerated inflammation-associated tissue pathology. This phenotype is characterized by loss of stemness, loss of goblet cells and mucus production, as well as sustained microbial dysbiosis, supporting the hypothesis that mitochondrial perturbations contribute to the pathogenesis of chronic inflammation. IBD is characterized by recurrent cycles of wounding and incomplete healing, making the ISC niche and its flexible adjustment of mitochondrial metabolism imperative for tissue regeneration[3]. In line, postoperative recurrence risk of Crohn's disease patients is linked to mitochondrial dysfunction in the ISC niche[16]. Persistent MT-UPR signaling associated with sustained expression of Hsp60 in the epithelium of IBD-related mouse models and patients[14] confirms a putative role of mitochondrial perturbation in chronic inflammation. ß-oxidation and subsequent OXPHOS is the primary energy source of bacteria-exposed colonocytes using microbiota-derived SCFA[3,24]. In line with metabolic reprogramming of the Hsp60-deficient epithelium towards glycolysis and reduced ATP production, colonic mitochondrial remodeling and adaption of energy production are reported to sustain mucosal healing after colitis[25].

Metabolic injury in Hsp60$^{\Delta/\Delta IEC}$ and Hsp60$^{\Delta/\Delta IEC}$;*Il10*$^{-/-}$ mice is absent in the distal colon of GF mice, highlighting the importance of microbial-metabolic circuits in inflammation-associated tissue injury. Studies identified a mechanistic role of microbial metabolites, including butyrate[2] and tryptophan[26]. However, tissue injury under Hsp60 deficiency is a cell-autonomous process in the small intestine and proximal colon, demonstrating compartmentalized effects of the microbial environment. Ido1 catabolizes the majority of luminal tryptophan and is expressed by immune cells[27] and epithelial cells[28]. Indeed, we observe Ido1 expression in crypts during metabolic injury. In line, Ido1 expression and elevated kynurenine levels positively correlate with GvHD severity[29] and IBD activity[30,31]. Using organoids, we demonstrate that Ido1 expression is elevated in response to pro-inflammatory cytokines. In addition, treatment with the kynurenine 3-HAA reduces stemness, amplifies MT-UPR signaling, reduces survival, and decreases ATP production, suggesting host-derived mechanisms contributing to metabolic injury. While 3-HAA can exert beneficial effects[32], it also possesses neurotoxic effects[33] and is described to reduce IL-10 production and thus hinder fine-tuning of immune homeostasis[34]. In

contrast, the kynurenine pathway also generates protective metabolites, whose conversion is reduced in IBD[19]. Interestingly, increased host-tryptophan utilization controls bacterial proliferation, conferring a competitive benefit for the host[35].

AhR is an environmental sensor playing a critical role in intestinal immunity and barrier function[36]. In line with our previous work[13], small intestinal injury appears at day 0 and is incompatible with the survival of animals lacking both AhR and Hsp60. Studies have reported beneficial effects of AhR activation in colitis mouse models by promoting regulatory profiles in T-cells[37,38] and IL-22 signaling[39]. Interestingly, IL22 deficiency does not worsen metabolic injury, excluding the role of IL22-mediated downstream AhR signals. As an alternative mechanism, we postulate that AhR deficiency synergizes with mitochondrial impairment by preventing the differentiation of repopulating IECs in response to metabolic injury in a bacterial-dependent manner. Loss of AhR in murine IECs is reported to reduce the differentiation capacity leading to impaired barrier function and increased lethality upon infection with *Citrobacter rodentium*[40]. Interestingly, microbiota profiling revealed a drop in species richness in Hsp60$^{\Delta/\Delta IEC}$;*AhR*$^{-/-}$ mice. More importantly, oral antibiotics exposure in these mice abrogates the lethal phenotype and dampens the severity of metabolic injury.

In line, Hsp60 deficiency in IECs triggers loss of bacterial richness and changes in the microbiota profile, particularly *B. caecimuris* expansion. Dysbiosis precedes the onset of tissue injury in Hsp60$^{\Delta/\Delta IEC}$ mice and persists in Hsp60$^{\Delta/\Delta IEC}$;*Il10*$^{-/-}$ mice, suggesting a causal relationship of microbe-host interactions. Selective colonization of GF Hsp60$^{\Delta/\Delta IEC}$ mice with OMM[12] recapitulates the injury phenotype and causes *B. caecimuris* expansion. Finally, mono-colonization with *B. caecimuris* induces metabolic injury, demonstrating a causal role of commensal bacteria in initiating epithelial injury in response to mitochondrial perturbation. These data confirm studies reporting gram-negative bacteria, including *Bacteroides*, to be enriched in IBD[41,42]. Elevated luminal oxygen is a characteristic feature in IBD patients, suggesting a putative mechanism for the dysbiosis in Hsp60$^{\Delta/\Delta IEC}$ and Hsp60$^{\Delta/\Delta IEC}$;*Il10*$^{-/-}$ mice. Interestingly, *A. muciniphila* is a commensal that abrogates metabolic injury in the presence of *B. caecimuris. A. muciniphila* degrades mucins to produce SCFA, in turn regulating mucus thickness and host energy substrates[43]. While healthy controls are associated with beneficial *Akkermansia* spp.[44], *A. muciniphila* is reportedly reduced in IBD patients[45].

In conclusion, we identified mitochondrial dysfunction as an underlying cause of tissue injury and the risk of recurrent inflammation in an IBD-susceptible host. Mitochondrial perturbation and bacterial signals cooperate in the development of metabolic injury, highlighting epithelial metabolism as an interface of microbe- and host-derived signals. Targeting specific mitochondrial pathways or microbe-host circuits may yield new therapeutic options in recurrent inflammatory pathologies in the intestine.

Funding

Funded by the Deutsche Forschungsgemeinschaft (DFG, German Research Foundation) – project number 395357507 (SFB 1371, Microbiome Signatures) and project number 469152594 (HA 3148/15-1 - Mitochondrial function in the regulation of intestinal tissue regeneration and inflammation-related pathologies).

Competing interests: None

The authors declare no competing interests.

Authors contributions

EU, DA, and DH designed the experiments, performed data analysis, and wrote the manuscript, ER provided support. EU, DA, and NM performed mouse experiments and respective mice tissue processing and analysis. EU performed organoid culture experiments. ER performed Microarray analysis. HO performed bacterial culture of minimal mouse consortia OMM[12], provided by BS. AM analyzed bacterial profiles in IBD fecal samples. SK and SJ performed Chipcytometry analyses of mice tissues, and DHB provided the facility. SR carried out shallow shotgun sequencing analysis. MR and KS performed histological evaluation of mice tissues. SH provided IL22ra1$^{-/-}$ mice. MA provided human IBD samples.

ORCID IDs

Elisabeth Urbauer https://orcid.org/0009-0003-5704-3589
Doriane Aguanno https://orcid.org/0000-0002-4154-3592
Amira Metwaly https://orcid.org/0000-0001-5740-0230
Marianne Remke https://orcid.org/0000-0002-1363-4737
Samuel Huber https://orcid.org/0000-0001-9325-8227
Matthieu Allez https://orcid.org/0000-0002-7269-5433
Eva Rath http://orcid.org/0000-0003-1910-1162
Dirk Haller http://orcid.org/0000-0002-6977-4085

References

1 Akdis, C. A. Does the epithelial barrier hypothesis explain the increase in allergy, autoimmunity and other chronic conditions? *Nat Rev Immunol* **21**, 739-751 (2021). https://doi.org:10.1038/s41577-021-00538-7

2 Roediger, W. E. The colonic epithelium in ulcerative colitis: an energy-deficiency disease? *Lancet* **2**, 712-715 (1980). https://doi.org:10.1016/s0140-6736(80)91934-0

3 Rath, E. & Haller, D. Intestinal epithelial cell metabolism at the interface of microbial dysbiosis and tissue injury. *Mucosal Immunology* **15**, 595-604 (2022). https://doi.org:10.1038/s41385-022-00514-x

4 Melber, A. & Haynes, C. M. UPR(mt) regulation and output: a stress response mediated by mitochondrial-nuclear communication. *Cell Res* **28**, 281-295 (2018). https://doi.org:10.1038/cr.2018.16

5 Hetz, C., Zhang, K. & Kaufman, R. J. Mechanisms, regulation and functions of the unfolded protein response. *Nature Reviews Molecular Cell Biology* **21**, 421-438 (2020). https://doi.org:10.1038/s41580-020-0250-z

6 Rath, E., Moschetta, A. & Haller, D. Mitochondrial function - gatekeeper of intestinal epithelial cell homeostasis. *Nat Rev Gastroenterol Hepatol* **15**, 497-516 (2018). https://doi.org:10.1038/s41575-018-0021-x

7 Metwaly, A., Reitmeier, S. & Haller, D. Microbiome risk profiles as biomarkers for inflammatory and metabolic disorders. *Nat Rev Gastroenterol Hepatol* **19**, 383-397 (2022). https://doi.org:10.1038/s41575-022-00581-2

8 Lloyd-Price, J. *et al.* Multi-omics of the gut microbial ecosystem in inflammatory bowel diseases. *Nature* **569**, 655-662 (2019). https://doi.org:10.1038/s41586-019-1237-9

9 Peled, J. U. *et al.* Microbiota as Predictor of Mortality in Allogeneic Hematopoietic-Cell Transplantation. *N Engl J Med* **382**, 822-834 (2020). https://doi.org:10.1056/NEJMoa1900623

10 Reitmeier, S. *et al.* Arrhythmic Gut Microbiome Signatures Predict Risk of Type 2 Diabetes. *Cell Host Microbe* **28**, 258-272 e256 (2020). https://doi.org:10.1016/j.chom.2020.06.004

11 Martínez, A. *et al.* Association of the organic cation transporter OCTN genes with Crohn's disease in the Spanish population. *Eur J Hum Genet* **14**, 222-226 (2006). https://doi.org:10.1038/sj.ejhg.5201529

12 Yu, X. *et al.* Association of UCP2 -866 G/A polymorphism with chronic inflammatory diseases. *Genes Immun* **10**, 601-605 (2009). https://doi.org:10.1038/gene.2009.29

13 Berger, E. *et al.* Mitochondrial function controls intestinal epithelial stemness and proliferation. *Nat Commun* **7**, 13171 (2016). https://doi.org:10.1038/ncomms13171

14 Rath, E. *et al.* Induction of dsRNA-activated protein kinase links mitochondrial unfolded protein response to the pathogenesis of intestinal inflammation. *Gut* **61**, 1269-1278 (2012). https://doi.org:10.1136/gutjnl-2011-300767

15 Jackson, D. N. *et al.* Mitochondrial dysfunction during loss of prohibitin 1 triggers Paneth cell defects and ileitis. *Gut* **69**, 1928-1938 (2020). https://doi.org:10.1136/gutjnl-2019-319523

16 Khaloian, S. *et al.* Mitochondrial impairment drives intestinal stem cell transition into dysfunctional Paneth cells predicting Crohn's disease recurrence. *Gut* **69**, 1939-1951 (2020). https://doi.org:10.1136/gutjnl-2019-319514

17 Rivera-Chávez, F. *et al.* Depletion of Butyrate-Producing Clostridia from the Gut Microbiota Drives an Aerobic Luminal Expansion of Salmonella. *Cell Host Microbe* **19**, 443-454 (2016). https://doi.org:10.1016/j.chom.2016.03.004

18 Rakoff-Nahoum, S., Paglino, J., Eslami-Varzaneh, F., Edberg, S. & Medzhitov, R. Recognition of commensal microflora by toll-like receptors is required for intestinal homeostasis. *Cell* **118**, 229-241 (2004). https://doi.org:10.1016/j.cell.2004.07.002

19 Michaudel, C. *et al.* Rewiring the altered tryptophan metabolism as a novel therapeutic strategy in inflammatory bowel diseases. *Gut* **72**, 1296-1307 (2023). https://doi.org:10.1136/gutjnl-2022-327337

20 Langhorst, J. *et al.* Comprehensive Lifestyle-Modification in Patients with Ulcerative Colitis-A Randomized Controlled Trial. *J Clin Med* **9** (2020). https://doi.org:10.3390/jcm9103087

21 Metwaly, A. *et al.* Integrated microbiota and metabolite profiles link Crohn's disease to sulfur metabolism. *Nat Commun* **11**, 4322 (2020). https://doi.org:10.1038/s41467-020-17956-1

22 Eberl, C. *et al.* Reproducible Colonization of Germ-Free Mice With the Oligo-Mouse-Microbiota in Different Animal Facilities. *Front Microbiol* **10**, 2999 (2019). https://doi.org:10.3389/fmicb.2019.02999

23 Brugiroux, S. *et al.* Genome-guided design of a defined mouse microbiota that confers colonization resistance against Salmonella enterica serovar Typhimurium. *Nat Microbiol* **2**, 16215 (2016). https://doi.org:10.1038/nmicrobiol.2016.215

24 Cook, S. I. & Sellin, J. H. Review article: short chain fatty acids in health and disease. *Aliment Pharmacol Ther* **12**, 499-507 (1998). https://doi.org:10.1046/j.1365-2036.1998.00337.x

25 Lan, A. *et al.* Mitochondrial remodeling and energy metabolism adaptations in colonic crypts during spontaneous epithelial repair after colitis induction in mice. *Free Radic Biol Med* **205**, 224-233 (2023). https://doi.org:10.1016/j.freeradbiomed.2023.06.007

26 Lamas, B. *et al.* CARD9 impacts colitis by altering gut microbiota metabolism of tryptophan into aryl hydrocarbon receptor ligands. *Nat Med* **22**, 598-605 (2016). https://doi.org:10.1038/nm.4102

27 Hwang, S. L., Chung, N. P., Chan, J. K. & Lin, C. L. Indoleamine 2, 3-dioxygenase (IDO) is essential for dendritic cell activation and chemotactic responsiveness to chemokines. *Cell Res* **15**, 167-175 (2005). https://doi.org:10.1038/sj.cr.7290282

28 Alvarado, D. M. *et al.* Epithelial Indoleamine 2,3-Dioxygenase 1 Modulates Aryl Hydrocarbon Receptor and Notch Signaling to Increase Differentiation of Secretory Cells and Alter Mucus-Associated Microbiota. *Gastroenterology* **157**, 1093-1108 e1011 (2019). https://doi.org:10.1053/j.gastro.2019.07.013

29 Landfried, K. *et al.* Tryptophan catabolism is associated with acute GVHD after human allogeneic stem cell transplantation and indicates activation of indoleamine 2,3-dioxygenase. *Blood* **118**, 6971-6974 (2011). https://doi.org:10.1182/blood-2011-06-357814

30 Nikolaus, S. *et al.* Increased Tryptophan Metabolism Is Associated With Activity of Inflammatory Bowel Diseases. *Gastroenterology* **153**, 1504-1516 e1502 (2017). https://doi.org:10.1053/j.gastro.2017.08.028

31 Proietti, E. *et al.* Modulation of Indoleamine 2,3-Dioxygenase 1 During Inflammatory Bowel Disease Activity in Humans and Mice. *Int J Tryptophan Res* **16**, 11786469231153109 (2023). https://doi.org:10.1177/11786469231153109

32 Krause, D. *et al.* The tryptophan metabolite 3-hydroxyanthranilic acid plays anti-inflammatory and neuroprotective roles during inflammation: role of hemeoxygenase-1. *Am J Pathol* **179**, 1360-1372 (2011). https://doi.org:10.1016/j.ajpath.2011.05.048

33 Chen, L. M. *et al.* Tryptophan-kynurenine metabolism: a link between the gut and brain for depression in inflammatory bowel disease. *J Neuroinflammation* **18**, 135 (2021). https://doi.org:10.1186/s12974-021-02175-2

34 Metghalchi, S. *et al.* Indoleamine 2,3-Dioxygenase Fine-Tunes Immune Homeostasis in Atherosclerosis and Colitis through Repression of Interleukin-10 Production. *Cell Metab* **22**, 460-471 (2015). https://doi.org:10.1016/j.cmet.2015.07.004

35 Le Floc'h, N., Otten, W. & Merlot, E. Tryptophan metabolism, from nutrition to potential therapeutic applications. *Amino Acids* **41**, 1195-1205 (2011). https://doi.org:10.1007/s00726-010-0752-7

36 Stockinger, B., Shah, K. & Wincent, E. AHR in the intestinal microenvironment: safeguarding barrier function. *Nature Reviews Gastroenterology & Hepatology* **18**, 559-570 (2021). https://doi.org:10.1038/s41575-021-00430-8

37 Aoki, R., Aoki-Yoshida, A., Suzuki, C. & Takayama, Y. Indole-3-Pyruvic Acid, an Aryl Hydrocarbon Receptor Activator, Suppresses Experimental Colitis in Mice. *The Journal of Immunology* **201**, 3683-3693 (2018). https://doi.org:10.4049/jimmunol.1701734

481 38 Ye, J. *et al.* The aryl hydrocarbon receptor preferentially marks and promotes gut regulatory T
482 cells. *Cell reports* **21**, 2277-2290 (2017).
483 39 Zelante, T. *et al.* Tryptophan catabolites from microbiota engage aryl hydrocarbon receptor
484 and balance mucosal reactivity via interleukin-22. *Immunity* **39**, 372-385 (2013).
485 40 Metidji, A. *et al.* The Environmental Sensor AHR Protects from Inflammatory Damage by
486 Maintaining Intestinal Stem Cell Homeostasis and Barrier Integrity. *Immunity* **49**, 353-362.e355
487 (2018). https://doi.org:https://doi.org/10.1016/j.immuni.2018.07.010
488 41 Andoh, A. *et al.* Comparison of the fecal microbiota profiles between ulcerative colitis and
489 Crohn's disease using terminal restriction fragment length polymorphism analysis. *J*
490 *Gastroenterol* **46**, 479-486 (2011). https://doi.org:10.1007/s00535-010-0368-4
491 42 Matsuda, H. *et al.* Characterization of antibody responses against rectal mucosa-associated
492 bacterial flora in patients with ulcerative colitis. *J Gastroenterol Hepatol* **15**, 61-68 (2000).
493 https://doi.org:10.1046/j.1440-1746.2000.02045.x
494 43 Liu, M. J. *et al.* Recent findings in Akkermansia muciniphila-regulated metabolism and its role
495 in intestinal diseases. *Clin Nutr* **41**, 2333-2344 (2022).
496 https://doi.org:10.1016/j.clnu.2022.08.029
497 44 Pisani, A. *et al.* Dysbiosis in the Gut Microbiota in Patients with Inflammatory Bowel Disease
498 during Remission. *Microbiol Spectr* **10**, e0061622 (2022).
499 https://doi.org:10.1128/spectrum.00616-22
500 45 Zhang, T. *et al.* Alterations of Akkermansia muciniphila in the inflammatory bowel disease
501 patients with washed microbiota transplantation. *Appl Microbiol Biotechnol* **104**, 10203-10215
502 (2020). https://doi.org:10.1007/s00253-020-10948-7
503 46 Dai, M. *et al.* Evolving gene/transcript definitions significantly alter the interpretation of
504 GeneChip data. *Nucleic Acids Research* **33**, e175-e175 (2005).
505 https://doi.org:10.1093/nar/gni179
506 47 Edgar, R. C. UPARSE: highly accurate OTU sequences from microbial amplicon reads. *Nat*
507 *Methods* **10**, 996-+ (2013). https://doi.org:10.1038/Nmeth.2604
508 48 Edgar, R. C., Haas, B. J., Clemente, J. C., Quince, C. & Knight, R. UCHIME improves sensitivity
509 and speed of chimera detection. *Bioinformatics* **27**, 2194-2200 (2011).
510 https://doi.org:10.1093/bioinformatics/btr381
511 49 Wang, Q., Garrity, G. M., Tiedje, J. M. & Cole, J. R. Naive Bayesian classifier for rapid assignment
512 of rRNA sequences into the new bacterial taxonomy. *Appl Environ Microb* **73**, 5261-5267
513 (2007). https://doi.org:10.1128/Aem.00062-07
514 50 Quast, C. *et al.* The SILVA ribosomal RNA gene database project: improved data processing and
515 web-based tools. *Nucleic Acids Research* **41**, D590-D596 (2013).
516 https://doi.org:10.1093/nar/gks1219
517 51 Lagkouvardos, I., Fischer, S., Kumar, N. & Clavel, T. Rhea: a transparent and modular R pipeline
518 for microbial profiling based on 16S rRNA gene amplicons. *Peerj* **5** (2017).
519 https://doi.org:10.7717/peerj.2836
520 52 Subramanian, B., Gao, S., Lercher, M. J., Hu, S. & Chen, W. H. Evolview v3: a webserver for
521 visualization, annotation, and management of phylogenetic trees. *Nucleic Acids Res* **47**, W270-
522 W275 (2019). https://doi.org:10.1093/nar/gkz357
523 53 Segata, N. *et al.* Metagenomic microbial community profiling using unique clade-specific
524 marker genes. *Nat Methods* **9**, 811-814 (2012). https://doi.org:10.1038/nmeth.2066

525

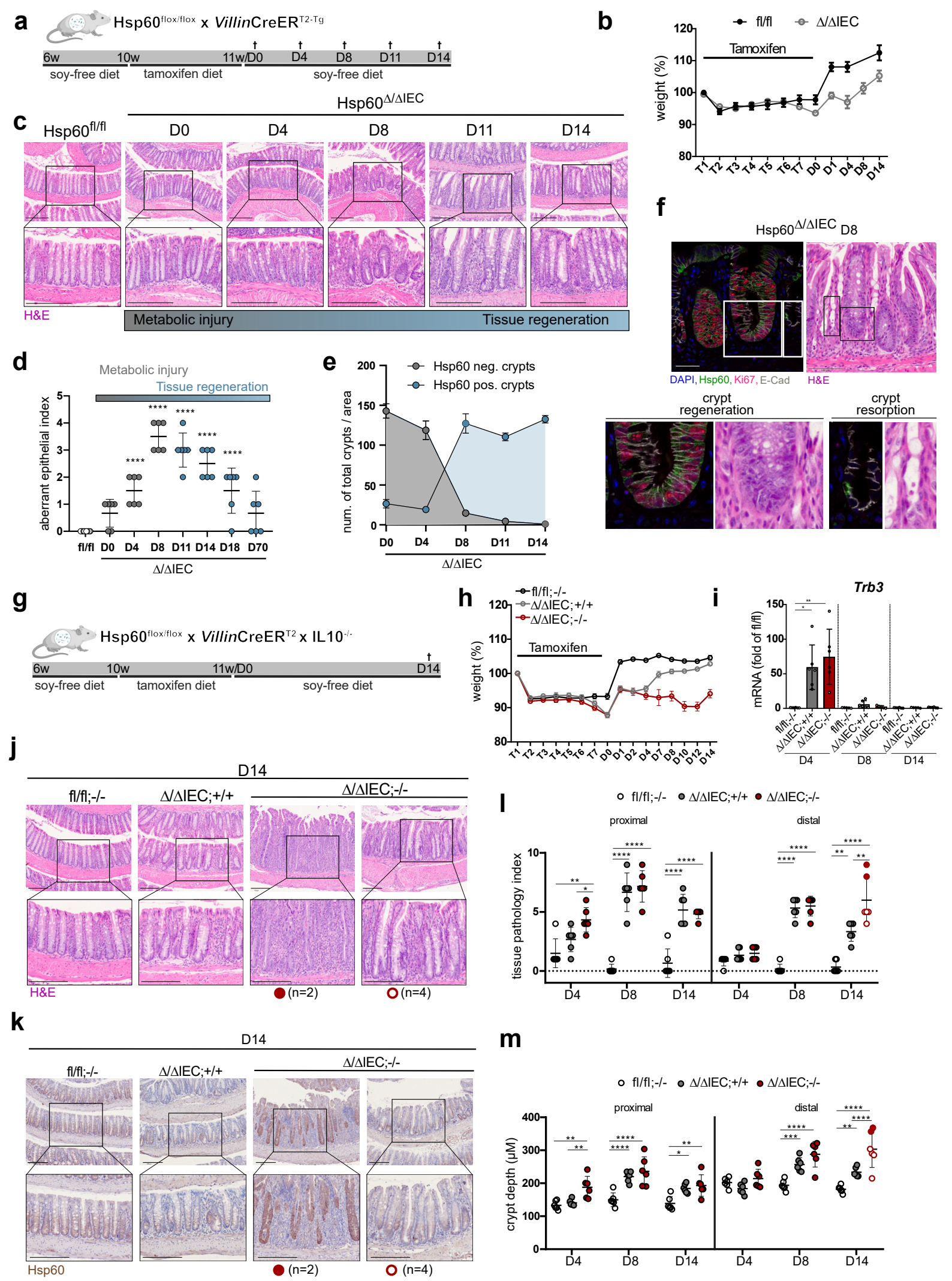
a
Hsp60flox/flox x VillinCreERT2-Tg
6w
10w
11w/D0
D4
D8
D11
D14
soy-free diet
tamoxifen diet
soy-free diet
b
fl/fl
Δ/ΔIEC
Tamoxifen
weight (%)
T1 T2 T3 T4 T5 T6 T7 D0 D1 D4 D8 D14
c
Hsp60Δ/ΔIEC
Hsp60fl/fl
D0
D4
D8
D11
D14
H&E
Metabolic injury
Tissue regeneration
d
Metabolic injury
Tissue regeneration
aberrant epithelial index
fl/fl D0 D4 D8 D11 D14 D18 D70
Δ/ΔIEC
e
Hsp60 neg. crypts
Hsp60 pos. crypts
num. of total crypts / area
D0 D4 D8 D11 D14
Δ/ΔIEC
f
Hsp60Δ/ΔIEC D8
DAPI, Hsp60, Ki67, E-Cad
H&E
crypt regeneration
crypt resorption
g
Hsp60flox/flox x VillinCreERT2 x IL10-/-
6w
10w
11w/D0
D14
soy-free diet
tamoxifen diet
soy-free diet
h
fl/fl;-/-
Δ/ΔIEC;+/+
Δ/ΔIEC;-/-
Tamoxifen
weight (%)
T1 T2 T3 T4 T5 T6 T7 D0 D1 D2 D4 D7 D8 D10 D12 D14
i
Trb3
mRNA (fold of fl/fl)
fl/fl;-/-
Δ/ΔIEC;+/+
Δ/ΔIEC;-/-
D4
D8
D14
j
D14
fl/fl;-/-
Δ/ΔIEC;+/+
Δ/ΔIEC;-/-
H&E
(n=2)
(n=4)
l
fl/fl;-/-
Δ/ΔIEC;+/+
Δ/ΔIEC;-/-
proximal
distal
tissue pathology index
D4 D8 D14 D4 D8 D14
k
D14
fl/fl;-/-
Δ/ΔIEC;+/+
Δ/ΔIEC;-/-
Hsp60
(n=2)
(n=4)
m
fl/fl;-/-
Δ/ΔIEC;+/+
Δ/ΔIEC;-/-
proximal
distal
crypt depth (µM)
D4 D8 D14 D4 D8 D14

Figure 1

Fig.1: Metabolic injury accelerates the onset of inflammation.

a, Experimental setup. Hsp60$^{fl/fl}$ x *Villin*CreER^{T2-Tg} mice (Hsp60$^{\Delta/\Delta IEC}$; Ctrl: Hsp60$^{fl/fl}$) were fed a soy-free diet for 4 weeks, followed by a tamoxifen diet at the age of 10 weeks for 7 days to induce Hsp60 deletion in IECs. Mice were sampled 0, 4, 8, 11, and 14 days after tamoxifen feeding and full Hsp60 deletion. **b,** Relative weight curve of Hsp60$^{\Delta/\Delta IEC}$ and Hsp60$^{fl/fl}$ mice from the start of tamoxifen feeding until sampling time point. **c,** Representative images of H&E staining of colonic tissue of Hsp60$^{\Delta/\Delta IEC}$ and Hsp60$^{fl/fl}$ mice from days 0 to 14. Scale bars: 200µm. **d,** H&E staining of colonic tissue of Hsp60$^{\Delta/\Delta IEC}$ and Hsp60$^{fl/fl}$ mice from days 0 to 70 were histologically scored for an aberrant epithelium. **e,** Quantification of Hsp60-negative and -positive crypts in Hsp60$^{\Delta/\Delta IEC}$ mice from days 0 to 14. **f,** Representative immunofluorescent co-staining of Hsp60 (green), Ki67 (red), E-Cadherin (grey), and DAPI (blue) as well as H&E staining of different crypt morphologies at day 8 in colonic tissue of Hsp60$^{\Delta/\Delta IEC}$ mice. Scale bar: 50µm. **g,** Experimental setup. Hsp60$^{fl/fl}$ x *Villin*CreER^{T2-Tg} x IL10$^{-/-}$ mice (Hsp60$^{\Delta/\Delta IEC}$;*Il10*$^{-/-}$; Ctrl: Hsp60$^{\Delta/\Delta IEC}$;*Il10*$^{+/+}$, Hsp60$^{fl/fl}$;*Il10*$^{-/-}$) were fed a soy-free diet for 4 weeks, followed by a tamoxifen diet at the age of 10 weeks for 7 days to induce Hsp60 deletion. Mice were sampled 4, 8, and 14 days after tamoxifen feeding and full Hsp60 deletion. **h,** Relative weight curve of Hsp60$^{\Delta/\Delta IEC}$;*Il10*$^{-/-}$, Hsp60$^{\Delta/\Delta IEC}$;*Il10*$^{+/+}$ and Hsp60$^{fl/fl}$;*Il10*$^{-/-}$ mice from the start of tamoxifen feeding until sampling time point. **i,** qPCR of the MT-UPR marker gene *Trb3* using mRNA of whole colonic tissue at days 4, 8, and 14 in Hsp60$^{\Delta/\Delta IEC}$;*Il10*$^{-/-}$ (Ctrl: Hsp60$^{\Delta/\Delta IEC}$;*Il10*$^{+/+}$, Hsp60$^{fl/fl}$;*Il10*$^{-/-}$) mice. **j, k** Representative images of (**j**) H&E staining and (**k**) immunohistochemistry staining of Hsp60 using colonic tissue of Hsp60$^{\Delta/\Delta IEC}$;*Il10*$^{-/-}$ (Ctrl: Hsp60$^{\Delta/\Delta IEC}$;*Il10*$^{+/+}$, Hsp60$^{fl/fl}$;*Il10*$^{-/-}$) mice at day 14. The brown color in (**k**) shows specific Hsp60 signal, and nuclei are stained with hematoxylin. Scale bars: 200µm. The red filled circles represent the two Hsp60$^{\Delta/\Delta IEC}$;*Il10*$^{-/-}$ mice with accelerated inflammation. The red open circles represent the four Hsp60$^{\Delta/\Delta IEC}$;*Il10*$^{-/-}$ mice without accelerated inflammation. **l, m** H&E stainings of colonic tissue (proximal vs. distal) of Hsp60$^{\Delta/\Delta IEC}$;*Il10*$^{-/-}$ (Ctrl: Hsp60$^{\Delta/\Delta IEC}$;*Il10*$^{+/+}$, Hsp60$^{fl/fl}$;*Il10*$^{-/-}$) mice from days 4, 8, and 14 were (**l**) histologically scored for inflammation and (**m**) crypt length was measured. Red filled and open circles as described in j.

Data are represented by (**b,h**) mean ± sem or (**d,e,i,l,m**) mean ± s.d. of six biological replicates. P-values were calculated by ANOVA followed by pairwise comparison testing (Tukey). *P<0.05, **P<0.01, ***P<0.001, ****P<0.0001.

D: day; Hsp60: heat shock protein 60; IECs: intestinal epithelial cells; H&E: hematoxylin and eosin; DAPI: 4′,6-diamidino-2-phenylindole; MT-UPR: mitochondrial unfolded protein response; Trb3: tribbles pseudokinase 3; IL10: interleukin-10.

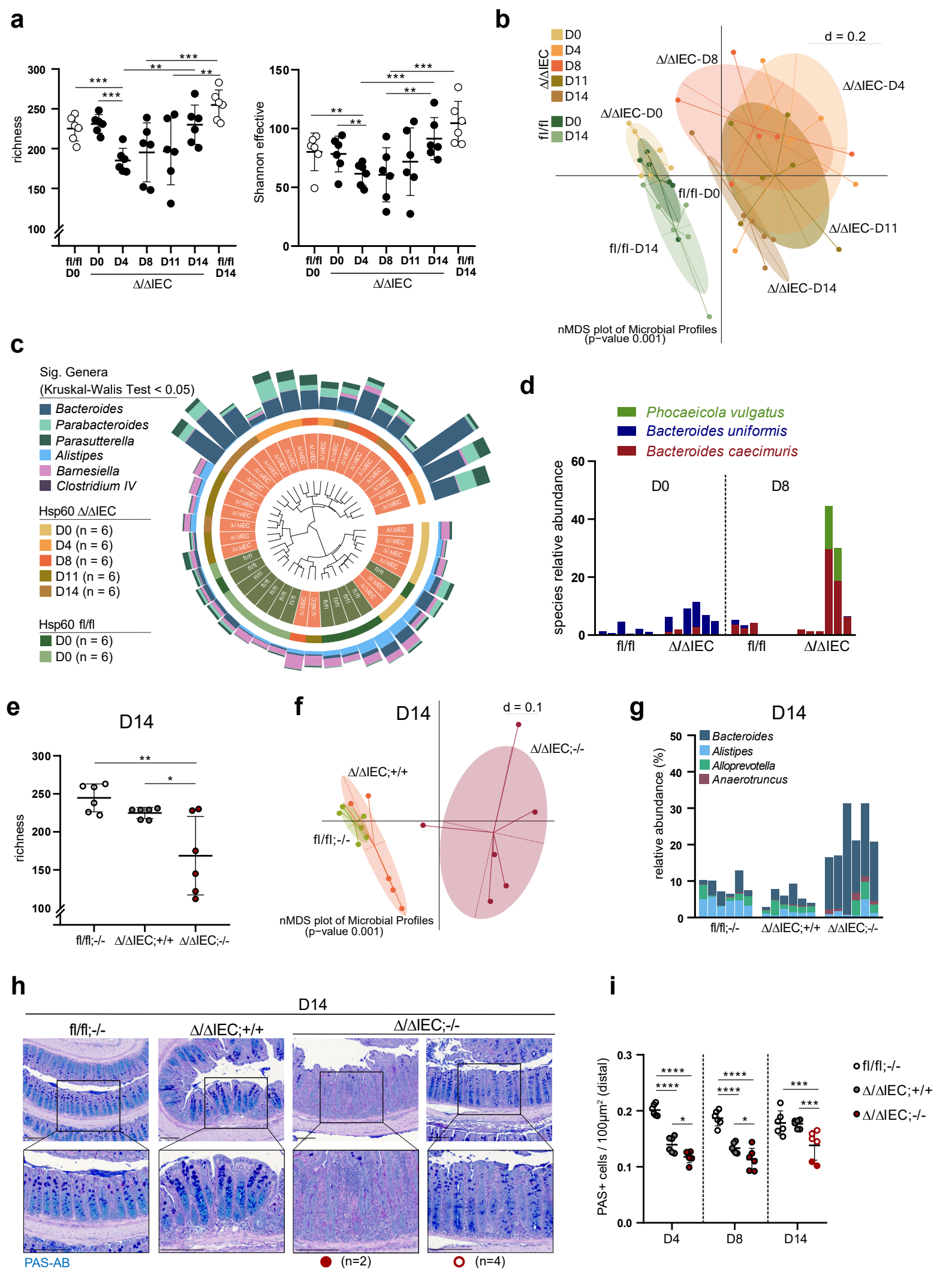
a
richness
Shannon effective
fl/fl D0
D0
D4
D8
D11
D14
fl/fl D14
Δ/ΔIEC
b
Δ/ΔIEC
D0
D4
D8
D11
D14
fl/fl
D0
D14
d = 0.2
Δ/ΔIEC-D8
Δ/ΔIEC-D4
Δ/ΔIEC-D0
fl/fl-D0
Δ/ΔIEC-D11
fl/fl-D14
Δ/ΔIEC-D14
nMDS plot of Microbial Profiles
(p−value 0.001)
c
Sig. Genera
(Kruskal-Walis Test < 0.05)
Bacteroides
Parabacteroides
Parasutterella
Alistipes
Barnesiella
Clostridium IV
Hsp60 Δ/ΔIEC
D0 (n = 6)
D4 (n = 6)
D8 (n = 6)
D11 (n = 6)
D14 (n = 6)
Hsp60 fl/fl
D0 (n = 6)
D0 (n = 6)
d
Phocaeicola vulgatus
Bacteroides uniformis
Bacteroides caecimuris
species relative abundance
D0
D8
fl/fl
Δ/ΔIEC
e
D14
richness
fl/fl;-/-
Δ/ΔIEC;+/+
Δ/ΔIEC;-/-
f
D14
d = 0.1
Δ/ΔIEC;-/-
Δ/ΔIEC;+/+
fl/fl;-/-
nMDS plot of Microbial Profiles
(p−value 0.001)
g
D14
Bacteroides
Alistipes
Alloprevotella
Anaerotruncus
relative abundance (%)
fl/fl;-/-
Δ/ΔIEC;+/+
Δ/ΔIEC;-/-
h
D14
fl/fl;-/-
Δ/ΔIEC;+/+
Δ/ΔIEC;-/-
PAS-AB
(n=2)
(n=4)
i
PAS+ cells / 100µm² (distal)
D4
D8
D14
fl/fl;-/-
Δ/ΔIEC;+/+
Δ/ΔIEC;-/-

Figure 2

Fig.2: Metabolic injury drives dysbiotic changes in the intestinal microbiota.

a, *Alpha*-diversity measured by richness and Shannon effective number of species in feces of Hsp60$^{\Delta/\Delta IEC}$ and Hsp60$^{fl/fl}$ mice from days 0 to 14. **b,** *Beta*-diversity depicted as nMDS plot of microbial profiles of fecal samples stratified by genotype (Hsp60$^{\Delta/\Delta IEC}$ and Hsp60$^{fl/fl}$ mice) and time point (day 0, 4, 8, 11, 14). **c,** Relative abundance of significantly enriched genera of the fecal microbiota in Hsp60$^{\Delta/\Delta IEC}$ and Hsp60$^{fl/fl}$ mice from days 0 to 14. The dendrogram depicts similarities between microbiota profiles based on generalized UniFrac distances between all 42 mice. Individual taxonomic composition of significantly altered genera is shown as stacked bar plots around the dendrogram. **d,** Shallow shotgun metagenomics of the fecal microbiota in Hsp60$^{\Delta/\Delta IEC}$ and Hsp60$^{fl/fl}$ mice at days 0 and 8. Species relative abundance of the three detected Bacteroides species, *B. caecimuris*, *B. uniformis,* and *P. vulgatus,* is shown. **e,** *Alpha*-diversity measured by species richness in feces of Hsp60$^{\Delta/\Delta IEC}$;*Il10*$^{-/-}$ (Ctrl: Hsp60$^{\Delta/\Delta IEC}$;*Il10*$^{+/+}$, Hsp60$^{fl/fl}$;*Il10*$^{-/-}$) mice at day 14. **f,** *Beta*-diversity depicted as nMDS plot of microbial profiles of fecal samples stratified by genotype (Hsp60$^{\Delta/\Delta IEC}$;*Il10*$^{-/-}$, Hsp60$^{\Delta/\Delta IEC}$;*Il10*$^{+/+,}$ Hsp60$^{fl/fl}$;*Il10*$^{-/-}$) at day 14. **g,** Relative abundance of significantly enriched genera in Hsp60$^{\Delta/\Delta IEC}$;*Il10*$^{-/-}$ (Ctrl: Hsp60$^{\Delta/\Delta IEC}$;*Il10*$^{+/+}$, Hsp60$^{fl/fl}$;*Il10*$^{-/-}$) mice at day 14. **h,** Representative images of PAS-AB staining in colonic tissue of Hsp60$^{\Delta/\Delta IEC}$;*Il10*$^{-/-}$ (Ctrl: Hsp60$^{\Delta/\Delta IEC}$;*Il10*$^{+/+}$ and Hsp60$^{fl/fl}$;*Il10*$^{-/-}$) mice at day 14. Acidic mucins are stained in cyan, neutral mucins in dark blue. Nuclei are stained with hematoxylin. Scale bars: 200µm. The red filled circles represent the two Hsp60$^{\Delta/\Delta IEC}$;*Il10*$^{-/-}$ mice with accelerated inflammation. The red open circles represent the four Hsp60$^{\Delta/\Delta IEC}$;*Il10*$^{-/-}$ mice without accelerated inflammation. **i,** Quantification of PAS-positive cells per 100µm^2 in distal colonic tissue of Hsp60$^{\Delta/\Delta IEC}$;*Il10*$^{-/-}$ (Ctrl: Hsp60$^{\Delta/\Delta IEC}$;*Il10*$^{+/+,}$ Hsp60$^{fl/fl}$;*Il10*$^{-/-}$) mice at days 4, 8, and 14.

(**a,e,i**) Data are represented by mean ± s.d. of six biological replicates. P-values were calculated by ANOVA followed by pairwise comparison testing (Tukey). *P<0.05, **P<0.01, ***P<0.001, ****P<0.0001. (**b,g**) Kruskal-Wallis test was used to select significant genera (P<0.05).

D: day; Hsp60: heat shock protein 60; IECs: intestinal epithelial cells; IL10: interleukin-10; PAS-AB: Alcian blue/Periodicacid-Schiff.

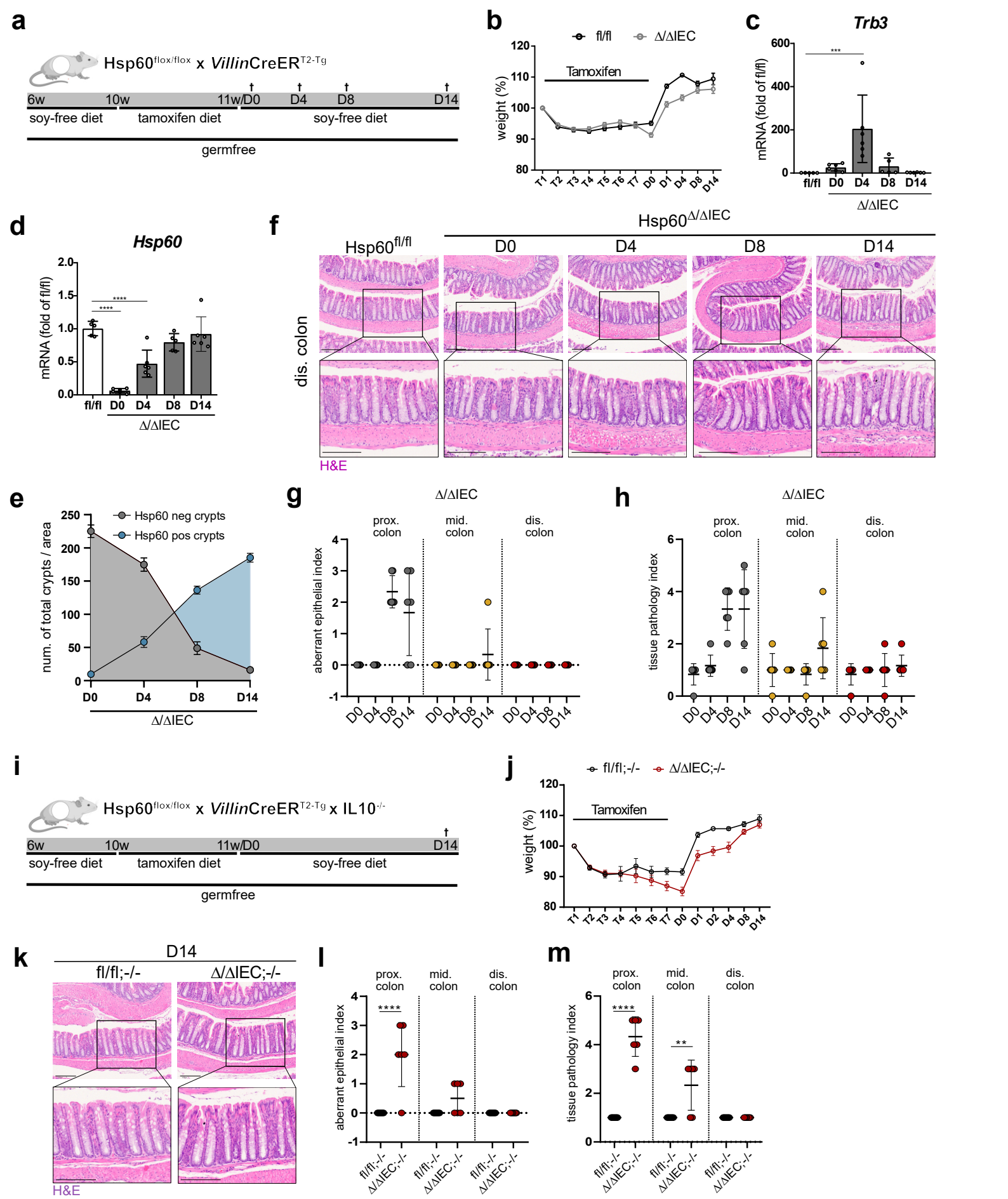
a
Hsp60flox/flox x VillinCreERT2-Tg
6w
10w
11w/D0
D4
D8
D14
soy-free diet
tamoxifen diet
soy-free diet
germfree
b
fl/fl
Δ/ΔIEC
Tamoxifen
weight (%)
c
Trb3
mRNA (fold of fl/fl)
d
Hsp60
mRNA (fold of fl/fl)
Δ/ΔIEC
e
Hsp60 neg crypts
Hsp60 pos crypts
num. of total crypts / area
f
Hsp60fl/fl
Hsp60Δ/ΔIEC
dis. colon
H&E
g
prox. colon
mid. colon
dis. colon
aberrant epithelial index
h
tissue pathology index
i
Hsp60flox/flox x VillinCreERT2-Tg x IL10-/-
j
fl/fl;-/-
Δ/ΔIEC;-/-
k
D14
fl/fl;-/-
Δ/ΔIEC;-/-
l
m

Figure 3

Fig.3: Bacteria control metabolic injury.

a, Experimental setup. GF Hsp60$^{fl/fl}$ x *Villin*CreER^{T2-Tg} mice (Hsp60$^{\Delta/\Delta IEC}$; Ctrl: Hsp60$^{fl/fl}$) were fed a soy-free diet for 4 weeks, followed by a tamoxifen diet at the age of 10 weeks for 7 days to induce Hsp60 deletion in IECs. Mice were sampled 0, 4, 8, and 14 days after tamoxifen feeding and full Hsp60 deletion. **b,** Relative weight curve of GF Hsp60$^{\Delta/\Delta IEC}$ and Hsp60$^{fl/fl}$ mice from the start of tamoxifen feeding until sampling time point. **c, d,** qPCR of (**c**) the MT-UPR marker gene *Trb3* and (**d**) the mitochondrial chaperone *Hsp60* using mRNA of whole colonic tissue from days 0 to 14 in GF Hsp60$^{\Delta/\Delta IEC}$ and Hsp60$^{fl/fl}$ mice. **e,** Quantification of Hsp60-negative and -positive crypts in GF Hsp60$^{\Delta/\Delta IEC}$ mice from days 0 to 14. **f,** Representative images of H&E staining of distal colonic tissue of GF Hsp60$^{\Delta/\Delta IEC}$ and Hsp60$^{fl/fl}$ mice at days 0 to 14. Scale bars: 200µm. **g, h,** H&E stainings of colonic tissue of GF Hsp60$^{\Delta/\Delta IEC}$ mice from days 0 to 14 were histologically scored for (**g**) an aberrant epithelium and (**h**) inflammation. The colonic swiss role was divided into three parts (proximal, middle and distal) and scored separately. **i,** GF Hsp60$^{fl/fl}$ x *Villin*CreER^{T2-Tg} x IL10$^{-/-}$ mice (Hsp60$^{\Delta/\Delta IEC}$;*Il10*$^{-/-}$; Ctrl: Hsp60$^{fl/fl}$;*Il10*$^{-/-}$) were fed a soy-free diet for 4 weeks, followed by a tamoxifen diet at the age of 10 weeks for 7 days to induce Hsp60 deletion. Mice were sampled 14 days after tamoxifen feeding and full Hsp60 deletion. **j,** Relative weight curve of GF Hsp60$^{\Delta/\Delta IEC}$;*Il10*$^{-/-}$ (Ctrl: Hsp60$^{fl/fl}$;*Il10*$^{-/-}$) mice from the start of tamoxifen feeding until sampling time point. **k,** Representative images of H&E staining of distal colonic tissue of GF Hsp60$^{\Delta/\Delta IEC}$;*Il10*$^{-/-}$ (Ctrl: Hsp60$^{fl/fl}$;*Il10*$^{-/-}$) mice at day 14. Scale bars: 200µm. **l, m,** H&E stainings of colonic tissue of GF Hsp60$^{\Delta/\Delta IEC}$;*Il10*$^{-/-}$ (Ctrl: Hsp60$^{fl/fl}$;*Il10*$^{-/-}$) mice from day 14 were histologically scored for (**l**) an aberrant epithelium and (**m**) inflammation. The colonic swiss role was divided into three parts (proximal, middle and distal) and scored separately.

Data are represented by (**b,j**) mean ± sem or (**c,d,e,g,h,l,m**) mean ± s.d. of six biological replicates. P-values were calculated by ANOVA followed by pairwise comparison testing (Tukey). *P<0.05, **P<0.01, ***P<0.001, ****P<0.0001.

GF: germfree; D: day; Hsp60: heat shock protein 60; IECs: intestinal epithelial cells; H&E: hematoxylin and eosin; MT-UPR: mitochondrial unfolded protein response; Trb3: tribbles pseudokinase 3; IL10: interleukin-10.

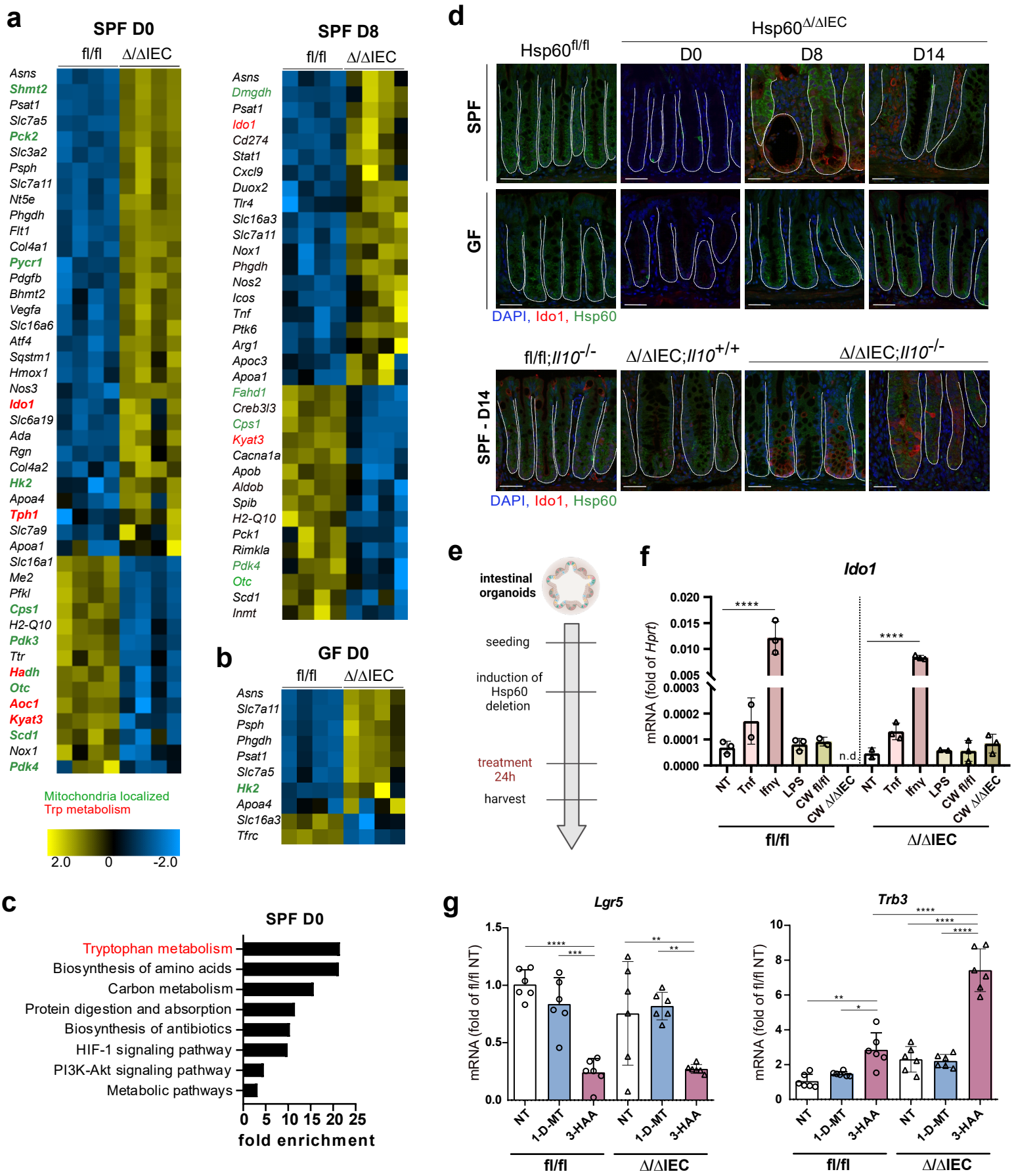
a
SPF D0
fl/fl
Δ/ΔIEC
Asns
Shmt2
Psat1
Slc7a5
Pck2
Slc3a2
Psph
Slc7a11
Nt5e
Phgdh
Flt1
Col4a1
Pycr1
Pdgfb
Bhmt2
Vegfa
Slc16a6
Atf4
Sqstm1
Hmox1
Nos3
Ido1
Slc6a19
Ada
Rgn
Col4a2
Hk2
Apoa4
Tph1
Slc7a9
Apoa1
Slc16a1
Me2
Pfkl
Cps1
H2-Q10
Pdk3
Ttr
Hadh
Otc
Aoc1
Kyat3
Scd1
Nox1
Pdk4
Mitochondria localized
Trp metabolism
2.0
0
-2.0
SPF D8
fl/fl
Δ/ΔIEC
Asns
Dmgdh
Psat1
Ido1
Cd274
Stat1
Cxcl9
Duox2
Tlr4
Slc16a3
Slc7a11
Nox1
Phgdh
Nos2
Icos
Tnf
Ptk6
Arg1
Apoc3
Apoa1
Fahd1
Creb3l3
Cps1
Kyat3
Cacna1a
Apob
Aldob
Spib
H2-Q10
Pck1
Rimkla
Pdk4
Otc
Scd1
Inmt
b
GF D0
fl/fl
Δ/ΔIEC
Asns
Slc7a11
Psph
Phgdh
Psat1
Slc7a5
Hk2
Apoa4
Slc16a3
Tfrc
d
Hsp60fl/fl
Hsp60Δ/ΔIEC
D0
D8
D14
SPF
GF
DAPI, Ido1, Hsp60
fl/fl;Il10-/-
Δ/ΔIEC;Il10+/+
Δ/ΔIEC;Il10-/-
SPF - D14
DAPI, Ido1, Hsp60
e
intestinal organoids
seeding
induction of Hsp60 deletion
treatment 24h
harvest
f
Ido1
mRNA (fold of Hprt)
0.020
0.015
0.010
0.005
0.0003
0.0002
0.0001
0.0000
****
****
n.d.
NT
Tnf
Ifnγ
LPS
CW fl/fl
CW Δ/ΔIEC
fl/fl
Δ/ΔIEC
c
SPF D0
Tryptophan metabolism
Biosynthesis of amino acids
Carbon metabolism
Protein digestion and absorption
Biosynthesis of antibiotics
HIF-1 signaling pathway
PI3K-Akt signaling pathway
Metabolic pathways
0
5
10
15
20
25
fold enrichment
g
Lgr5
mRNA (fold of fl/fl NT)
1.5
1.0
0.5
0.0
****
***
**
**
NT
1-D-MT
3-HAA
fl/fl
Δ/ΔIEC
Trb3
mRNA (fold of fl/fl NT)
10
8
6
4
2
0
**
*
****
****
****
NT
1-D-MT
3-HAA
fl/fl
Δ/ΔIEC

Figure 4

Fig.4: Host-tryptophan metabolism is rewired during metabolic injury.

a, b, Heatmap of a NanoString® analysis using a metabolic panel of ~ 800 genes in mRNA from whole colonic tissue in Hsp60$^{\Delta/\Delta IEC}$ and Hsp60$^{fl/fl}$ mice under (**a**) SPF or (**b**) GF housing at days 0 and/or 8 after Hsp60 deletion. Depicted are genes with a fold-change greater than ± 2. Genes encoding mitochondria-localized proteins are colored in green, tryptophan metabolism-associated genes in red. **c,** KEGG pathway analysis of the 45 altered genes in Hsp60$^{\Delta/\Delta IEC}$ mice under SPF conditions at day 0. Only pathways with a significant False Discovery Rate and at least 5 genes mapping to a pathway were selected. **d,** Representative immunofluorescent co-staining of Hsp60 (green), Ido1 (red), and DAPI (blue) in distal colonic tissue. Upper panel: Hsp60$^{\Delta/\Delta IEC}$ and Hsp60$^{fl/fl}$ mice under SPF or GF housing from days 0 to 14. Lower panel: Hsp60$^{\Delta/\Delta IEC}$;*Il10*$^{-/-}$ (Ctrl: Hsp60$^{\Delta/\Delta IEC}$;*Il10*$^{+/+}$, Hsp60$^{fl/fl}$;*Il10*$^{-/-}$) mice under SPF housing at day 14. Scale bars: 50 µm. **e,** Experimental setup. Small intestinal crypts were isolated and seeded in Matrigel®, followed by Hsp60 deletion *ex vivo* via tamoxifen addition to the media. Organoids were treated 4 or 5 days after Hsp60 deletion for 24h or 48h, respectively. **f,** qPCR of *Ido1* using mRNA of organoids at day 6 after Hsp60 deletion that were treated with Tnf, Ifnγ, LPS or cecal water (from Hsp60$^{\Delta/\Delta IEC}$ or Hsp60$^{fl/fl}$ mice at day 8) for 24h. **g,** qPCR of the stemness marker gene *Lgr5* and the MT-UPR marker gene *Trb3* using mRNA of organoids at day 6 after Hsp60 deletion that were treated with the Ido1 antagonist 1-D-MT or the Ido1 agonist 3-HAA for 48h.

(**a,b,c**) Data include four biological replicates. (**f,g**) Data are represented by mean ± s.d. of (**f**) three / (**g**) six technical replicates. P-values were calculated by ANOVA followed by pairwise comparison testing (Tukey). *P<0.05, **P<0.01, ***P<0.001, ****P<0.0001.

SPF: specific-pathogen-free; GF: germfree; D: day; Hsp60: heat shock protein 60; IECs: intestinal epithelial cells; Ido1: indoleamine 2, 3-dioxygenase 1; DAPI: 4′,6-diamidino-2-phenylindole; IL10: interleukin-10; Tnf: tumor necrosis factor; Ifnγ: interferon γ; LPS: lipopolysaccharide; CW: cecal water; 1-D-MT: dimethyltryptamine, 3-HAA: 3-hydroxyanthranilic acid; MT-UPR: mitochondrial unfolded protein response; Trb3: tribbles pseudokinase 3; Lgr5: leucine-rich repeat-containing G-protein coupled receptor 5.

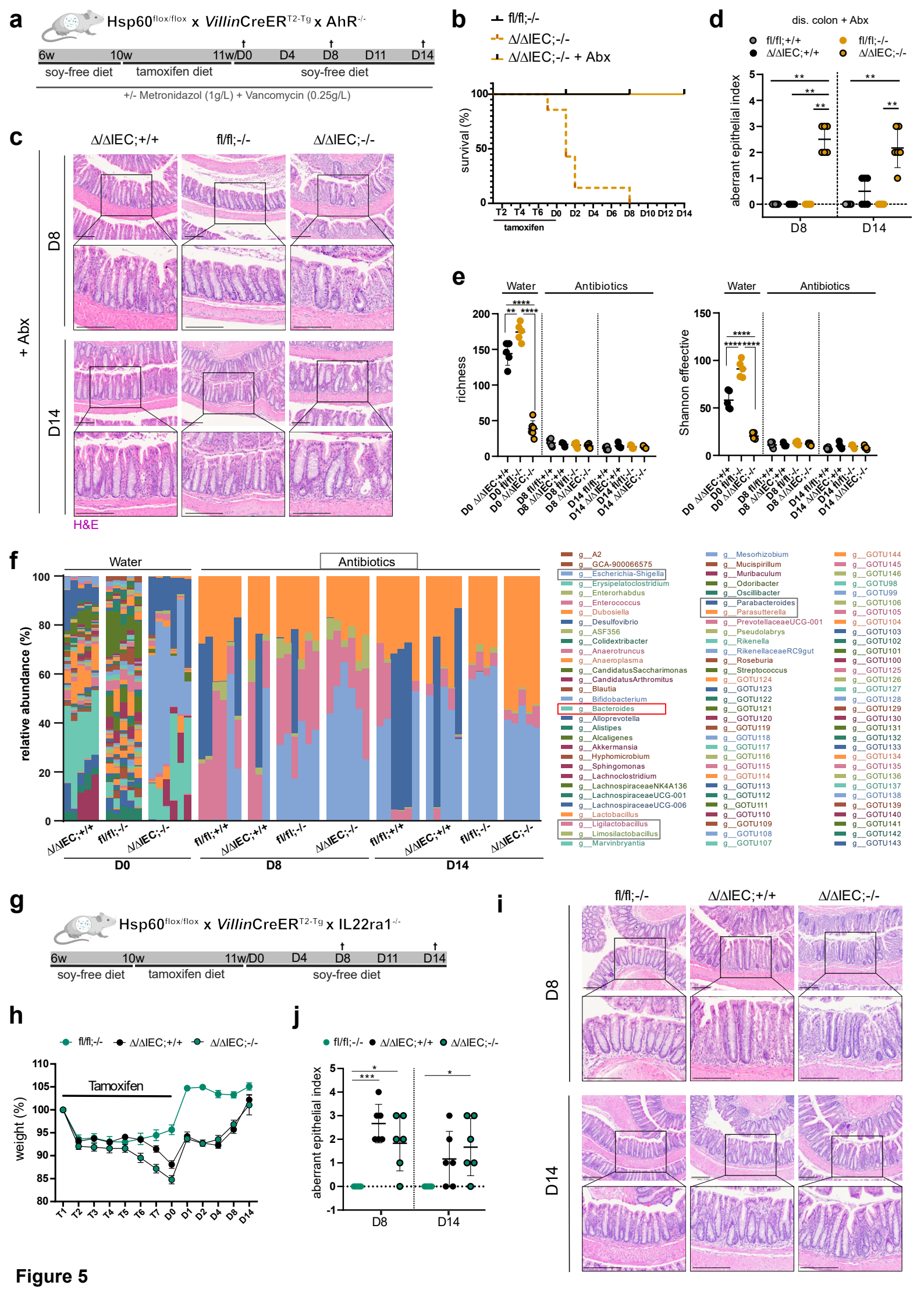
a
Hsp60flox/flox x VillinCreERT2-Tg x AhR-/-
6w
10w
11w/D0
D4
D8
D11
D14
soy-free diet
tamoxifen diet
soy-free diet
+/- Metronidazol (1g/L) + Vancomycin (0.25g/L)
b
fl/fl;-/-
Δ/ΔIEC;-/-
Δ/ΔIEC;-/- + Abx
survival (%)
tamoxifen
d
dis. colon + Abx
fl/fl;+/+
Δ/ΔIEC;+/+
fl/fl;-/-
Δ/ΔIEC;-/-
aberrant epithelial index
D8
D14
c
Δ/ΔIEC;+/+
fl/fl;-/-
Δ/ΔIEC;-/-
+ Abx
D8
D14
H&E
e
Water
Antibiotics
richness
Shannon effective
f
Water
Antibiotics
relative abundance (%)
D0
D8
D14
g
Hsp60flox/flox x VillinCreERT2-Tg x IL22ra1-/-
6w
10w
11w/D0
D4
D8
D11
D14
soy-free diet
tamoxifen diet
soy-free diet
h
fl/fl;-/-
Δ/ΔIEC;+/+
Δ/ΔIEC;-/-
Tamoxifen
weight (%)
j
fl/fl;-/-
Δ/ΔIEC;+/+
Δ/ΔIEC;-/-
aberrant epithelial index
D8
D14
i
fl/fl;-/-
Δ/ΔIEC;+/+
Δ/ΔIEC;-/-
D8
D14

Figure 5

Fig.5: Ahr signaling is a protective mechanism against metabolic injury

a, Experimental setup. Hsp60$^{fl/fl}$ x *Villin*CreER^{T2-Tg} x AhR$^{-/-}$ mice (Hsp60$^{\Delta/\Delta IEC}$;*AhR*$^{-/-}$; Ctrl: Hsp60$^{\Delta/\Delta IEC}$;*AhR*$^{+/+}$, Hsp60$^{fl/fl}$;*Ahr*$^{-/-}$) were fed a soy-free diet for 4 weeks, followed by a tamoxifen diet at the age of 10 weeks for 7 days to induce Hsp60 deletion. In addition, mice were treated with Abx (Metronidazole (1g/L) and Vancomycin (0.25g/L)) from 6 weeks on. Mice were sampled at days 0, 8, and 14 days after tamoxifen feeding and full Hsp60 deletion. In addition, to a control cohort (water) sampled at day 0, animals exposed to water were either sampled at day 8 (Ctrl: Hsp60$^{\Delta/\Delta IEC}$;*AhR*$^{+/+}$, Hsp60$^{fl/fl}$;*Ahr*$^{-/-}$) or when reaching abortion criteria for Hsp60$^{\Delta/\Delta IEC}$;*AhR*$^{-/-}$ mice. **b,** Survival (%) of Hsp60$^{\Delta/\Delta IEC}$;*AhR*$^{-/-}$ mice treated with or without Abx (Ctrl: Hsp60$^{fl/fl}$;*AhR*$^{-/-}$) from start of tamoxifen treatment until day 14. **c,** Representative images of H&E staining of distal colonic tissue of Hsp60$^{\Delta/\Delta IEC}$;*AhR*$^{-/-}$ mice (Ctrl: Hsp60$^{\Delta/\Delta IEC}$;*AhR*$^{+/+}$, Hsp60$^{fl/fl}$;*Ahr*$^{-/-}$) at days 8 and 14 treated with Abx. Scale bars: 200µm. **d,** H&E stainings of distal colonic tissue of Hsp60$^{\Delta/\Delta IEC}$;*AhR*$^{-/-}$ mice (Ctrl: Hsp60$^{\Delta/\Delta IEC}$;*AhR*$^{+/+}$, Hsp60$^{fl/fl}$;*Ahr*$^{-/-}$) at days 8 and 14 treated with Abx were histologically scored for an aberrant epithelium. **e,** *Alpha*-diversity measured by richness and Shannon effective number of species in feces of Hsp60$^{\Delta/\Delta IEC}$;*AhR*$^{-/-}$ mice (Ctrl: Hsp60$^{\Delta/\Delta IEC}$;*AhR*$^{+/+}$, Hsp60$^{fl/fl}$;*Ahr*$^{-/-}$) treated with (day 8 and 14) or without antibiotics (day 0). **f,** Relative abundance of different genera of the fecal microbiota in Hsp60$^{\Delta/\Delta IEC}$;*AhR*$^{-/-}$ mice (Ctrl: Hsp60$^{\Delta/\Delta IEC}$;*AhR*$^{+/+}$, Hsp60$^{fl/fl}$;*Ahr*$^{-/-}$) treated with (day 8 and 14) or without Abx (day 0). A grey rectangle frames genera still present with Abx treatment. High abundant genera, which disappear with Abx treatment, are framed by a red rectangle. **g,** Experimental setup. Hsp60$^{fl/fl}$ x *Villin*CreER^{T2-Tg} x IL22ra1$^{-/-}$ mice (Hsp60$^{\Delta/\Delta IEC}$;*Il22ra1*$^{-/-}$; Ctrl: Hsp60$^{\Delta/\Delta IEC}$;*Il22ra1*$^{+/+}$, Hsp60$^{fl/fl}$;*Il22ra1*$^{-/-}$) were fed a soy-free diet for 4 weeks, followed by a tamoxifen diet at the age of 10 weeks for 7 days to induce Hsp60 deletion. Mice were sampled at days 8 and 14 days after tamoxifen feeding and full Hsp60 deletion. **h,** Relative weight curve of Hsp60$^{\Delta/\Delta IEC}$;*Il22ra1*$^{-/-}$ mice (Ctrl: Hsp60$^{\Delta/\Delta IEC}$;*Il22ra1*$^{+/+}$, Hsp60$^{fl/fl}$;*Il22ra1*$^{-/-}$) from the start of tamoxifen feeding until sampling time point. **i, j,** (**i**) Representative images of H&E staining and (**j**) histological scoring for an aberrant epithelium of distal colonic tissue of Hsp60$^{\Delta/\Delta IEC}$;*Il22ra1*$^{-/-}$ mice (Ctrl: Hsp60$^{\Delta/\Delta IEC}$;*Il22ra1*$^{+/+}$, Hsp60$^{fl/fl}$;*Il22ra1*$^{-/-}$) at day 8 and 14. Scale bars: 200µm. **j,** H&E stainings of distal colonic tissue of Hsp60$^{\Delta/\Delta IEC}$;*IL22ra1*$^{-/-}$ (Ctrl: Hsp60$^{\Delta/\Delta IEC}$;*Il22ra1*$^{+/+}$, Hsp60$^{fl/fl}$;*Il22ra1*$^{-/-}$) mice at days 8 and 14 were histologically scored for an aberrant epithelium.

Data are represented by (**h**) mean ± sem or (**d,e,j**) mean ± s.d. of six biological replicates. (**e,j**) P-values were calculated by ANOVA followed by pairwise comparison testing (Tukey). (**d**) P-values were calculated by Kruskal-Wallis followed by Dunn's post-test comparisons. *P<0.05, **P<0.01, ***P<0.001, ****P<0.0001.

Hsp60: heat shock protein 60; IECs: intestinal epithelial cells; AhR: aryl hydrocarbon receptor; Abx: antibiotics; Il22ra1: interleukin 22 receptor alpha 1; H&E: hematoxylin and eosin.

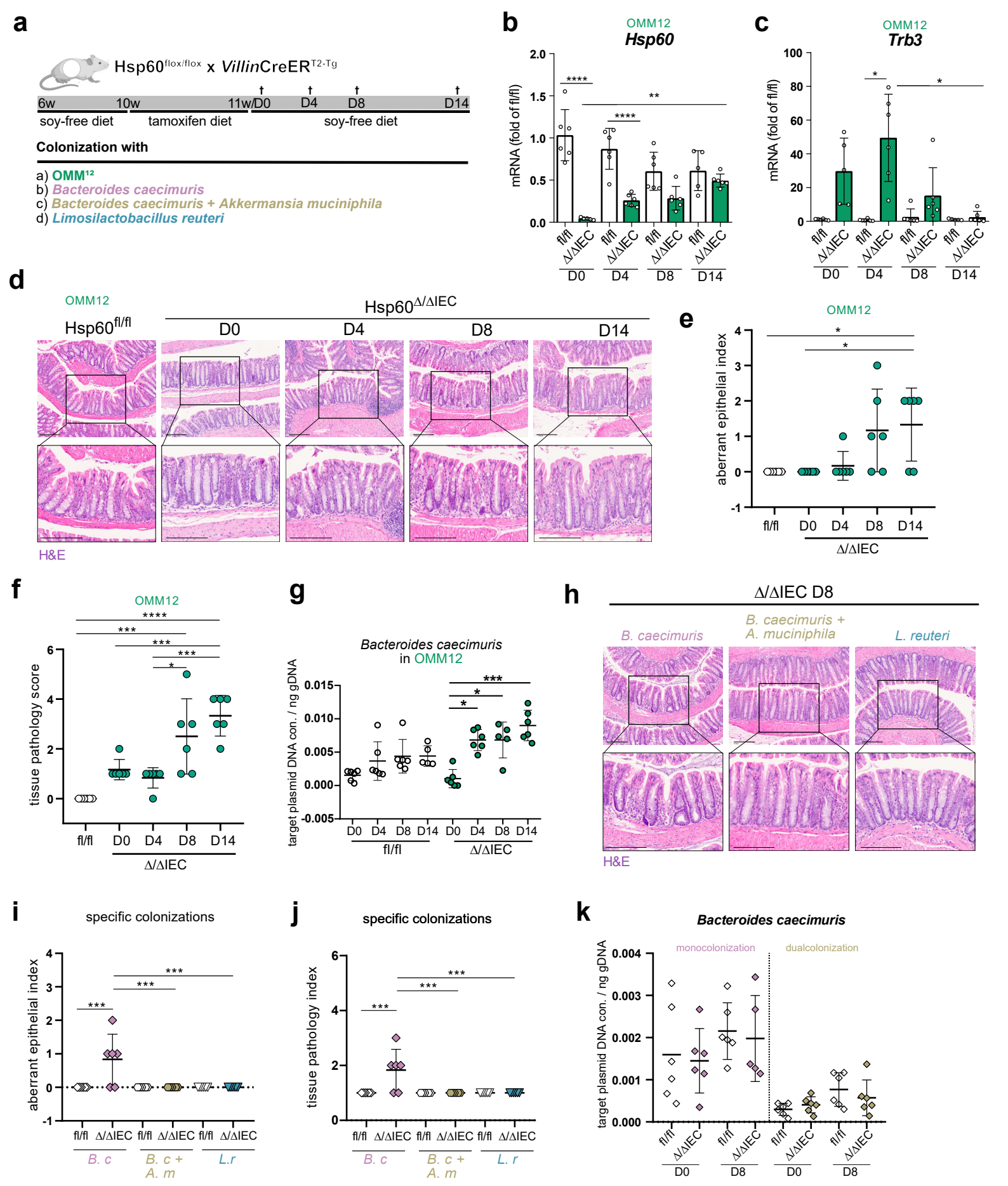
a
Hsp60flox/flox x VillinCreERT2-Tg
6w
10w
11w/D0
D4
D8
D14
soy-free diet
tamoxifen diet
soy-free diet
Colonization with
a) OMM12
b) Bacteroides caecimuris
c) Bacteroides caecimuris + Akkermansia muciniphila
d) Limosilactobacillus reuteri
b
OMM12
Hsp60
mRNA (fold of fl/fl)
c
OMM12
Trb3
mRNA (fold of fl/fl)
fl/fl
Δ/ΔIEC
D0
D4
D8
D14
d
OMM12
Hsp60fl/fl
Hsp60Δ/ΔIEC
D0
D4
D8
D14
H&E
e
OMM12
aberrant epithelial index
fl/fl
D0
D4
D8
D14
Δ/ΔIEC
f
OMM12
tissue pathology score
fl/fl
D0
D4
D8
D14
Δ/ΔIEC
g
Bacteroides caecimuris
in OMM12
target plasmid DNA con. / ng gDNA
D0
D4
D8
D14
fl/fl
Δ/ΔIEC
h
Δ/ΔIEC D8
B. caecimuris
B. caecimuris +
A. muciniphila
L. reuteri
H&E
i
specific colonizations
aberrant epithelial index
fl/fl
Δ/ΔIEC
B. c
B. c +
A. m
L.r
j
specific colonizations
tissue pathology index
fl/fl
Δ/ΔIEC
B. c
B. c +
A. m
L. r
k
Bacteroides caecimuris
monocolonization
dualcolonization
target plasmid DNA con. / ng gDNA
fl/fl
Δ/ΔIEC
D0
D8

Figure 6

Fig.6: *Bacteroides caecimuris* induces metabolic injury.

a, Experimental setup. GF Hsp60$^{fl/fl}$ x *Vil*CreER^{T2} mice (Hsp60$^{\Delta/\Delta IEC}$; Ctrl: Hsp60$^{fl/fl}$) were rectally gavaged twice at the age of 6 weeks with a) the Oligo-Mouse-Microbiota (OMM^{12}) synthetic bacterial community b) *Bacteroides caecimuris*, c) *Bacteroides caecimuris* and *Akkermansia muciniphila* or d) *Limosilactobacillus reuteri*. Mice were fed a soy-free diet for 4 weeks, followed by a tamoxifen diet at the age of 10 weeks for 7 days to induce Hsp60 deletion in IECs. Mice were sampled on different days after tamoxifen feeding and full Hsp60 deletion. **b, c,** qPCR of (**b**) the mitochondrial chaperone *Hsp60* and (**c**) the MT-UPR marker gene *Trb3* using mRNA of whole colonic tissue of GF Hsp60$^{\Delta/\Delta IEC}$ and Hsp60$^{fl/fl}$ mice colonized with OMM^{12} from days 0 to 14. **d,** Representative images of H&E staining of distal colonic tissue of GF Hsp60$^{\Delta/\Delta IEC}$ and Hsp60$^{fl/fl}$ mice colonized with OMM^{12} from days 0 to 14. Scale bars: 200µm. **e, f,** H&E stainings of distal colonic tissue of GF Hsp60$^{\Delta/\Delta IEC}$ and Hsp60$^{fl/fl}$ mice colonized with OMM^{12} were histologically scored for (**e**) an aberrant epithelium and (**f**) inflammation from days 0 to 14. **g,** Abundance of *B. caecimuris* in feces of GF Hsp60$^{\Delta/\Delta IEC}$ and Hsp60$^{fl/fl}$ mice colonized with OMM^{12} quantified by 16S targeted qPCR from days 0 to 14. **h,** Representative images of H&E staining of distal colonic tissue of GF Hsp60$^{\Delta/\Delta IEC}$ mice colonized with *B. caecimuris, B. caecimuris* and *A. muciniphila* or *L. reuteri* at day 8. Scale bars: 200µm. **i, j,** H&E stainings of distal colonic tissue of GF Hsp60$^{\Delta/\Delta IEC}$ mice colonized with *B. caecimuris, B. caecimuris* and *A. muciniphila* or *L. reuteri* were histologically scored for (**i**) an aberrant epithelium and (**j**) inflammation at day 8 after Hsp60 deletion. **k,** Abundance of *B. caecimuris* in feces of GF Hsp60$^{\Delta/\Delta IEC}$ and Hsp60$^{fl/fl}$ mice colonized with *B. caecimuris* or *B. caecimuris* and *A. muciniphila* quantified by 16S targeted qPCR at days 0 and 8.

(**b,c,e,f,g,i,j,k**) Data are represented by mean ± s.d. of six biological replicates. P-values were calculated by ANOVA followed by pairwise comparison testing (Tukey). *P<0.05, **P<0.01, ***P<0.001, ****P<0.0001.

GF: germfree; D: day; Hsp60: heat shock protein 60; IECs: intestinal epithelial cells; MT-UPR: mitochondrial unfolded protein response; Trb3: tribbles pseudokinase 3; H&E: hematoxylin and eosin.

Online Methods

Ethics statement. All animal experiments, as well as maintenance and breeding of mouse lines, were approved by the Committee on Animal Health Care and Use of the state of Upper Bavaria (Regierung von Oberbayern; AZ ROB-55.2-2532.Vet_02-14-217, AZ ROB-55.2-2532.Vet_02-20-58, AZ ROB-55.2-2532.Vet_02-18-37) and performed in strict compliance with the EEC recommendations for the care and use of laboratory animals (European Communities Council Directive of November 24, 1986 (86/609/EEC)).

Human cohorts. Microbial profiling of stool samples derived from 3 IBD patient cohorts were included: French Biotherapy cohort (N=147) and the two previously published Spanish HSCT cohort (N=153)[21], and German UC cohort (N=168)[20]. The Enable cohort (PMID: 33195372 and PMID: 32619440), including healthy non-smoking individuals at different phases of life, recruited in Freising (Southern Germany) (N=817), was included for comparison. The Biotherapy cohort is a longitudinal cohort comprising a total of 80 patients with IBD (CD: N=41, UC: N=39) who were treated with biological therapy (CD patients: Infliximab N=9, Vedolizumab N=5, Ustekinumab N=12, Adalimumab N=13, NA=2; UC patients: Infliximab N=11, Vedolizumab N=10, Golimumab N=9, Adalimumab N=2, NA=7). Clinical disease monitoring and sampling were performed at three time points (weeks 0, 14, and 52 after treatment). This study was conducted by Prof. Matthieu Allez at the Hôpital Saint-Louis in Paris (NCT: 02693340). All study methods were approved by the ethics committee of the hospital and complied with all relevant ethical regulations for studies with human research participants. Written informed consent was obtained from all subjects.

Animals and housing conditions. Hsp60$^{flox/flox}$ mice and Hsp60$^{flox/flox}$ x *Villin*CreER$^{T2\text{-}Tg}$ mice (to generate IEC-specific Hsp60 knockout mice via tamoxifen induction (Hsp60$^{\Delta/\Delta IEC}$)) were generated as described previously[13]. In addition, Hsp60$^{\Delta/\Delta IEC}$ mice were crossed with whole body IL-10 knockout mice (*Il10*$^{-/-}$), AhR knockout mice (*AhR*$^{-/-}$) and IL22ra1 knockout mice (*Il22ra1*$^{-/-}$) to generate Hsp60$^{\Delta/\Delta IEC}$;*Il10*$^{-/-}$, Hsp60$^{\Delta/\Delta IEC}$;*AhR*$^{-/-}$ and Hsp60$^{\Delta/\Delta IEC}$;*Il22ra1*$^{-/-}$ mice. All mice were housed under specific pathogen-free (SPF) or germfree (GF) conditions according to the criteria of the Federation for Laboratory Animal Science Associations (FELASA) (12h light/dark cycles at 24–26°C) in the mouse facility at the Technical University of Munich (School of Life Sciences Weihenstephan). GF mice were housed in flexible film isolators ventilated via HEPA-filtered air at 22 ± 1°C. All mice received a standard diet (autoclaved V1124-300, Ssniff) *ad libitum*, autoclaved water and were sacrificed by CO_2 or isoflurane. GF status was controlled by cultivating feces in Columbia Agar with 5% Sheep Blood (BD^{TM}) before the start of the experiments and at sampling time points.

Induction of postnatal recombination and monitoring of mice. For conditional *Hsp60* deletion, 6 weeks old male Hsp60$^{flox/flox}$ x *Villin*CreER$^{T2\text{-}Tg}$, Hsp60$^{flox/flox}$ x *Villin*CreER$^{T2\text{-}Tg}$ x

IL10$^{-/-}$, Hsp60$^{flox/flox}$ x *Villin*CreER^{T2-Tg} x AhR$^{-/-}$ and Hsp60$^{flox/flox}$ x *Villin*CreER^{T2-Tg} x IL22ra1$^{-/-}$ mice and appropriate control mice were kept on phytoestrogen-reduced diet (V1154-300, Ssniff) for four weeks under SPF or GF conditions. Afterwards, mice received 400mg tamoxifen citrate per kg chow feed (CreActive T400 (10mm, Rad), Genobios) *ad libitum* for 7 days. After the induction phase, tamoxifen diet was replaced with the phytoestrogen-reduced diet. During and after the induction phase, mice were monitored daily and aborted when a combined score considering weight loss, changes in stool consistency, general behavior, and general state of health was reached. Animals were sacrificed at the indicated time points.

Selective colonizations of germfree mice. For selective colonizations, GF Hsp60$^{flox/flox}$ x *Villin*CreER^{T2-Tg} and Hsp60$^{flox/flox}$ x *Villin*CreER^{T2-Tg} x IL10$^{-/-}$ mice and their appropriate control mice were rectally gavaged (two times) using 20 Gauge gavage needles (Fine Science Tools) at the age of 6 weeks with the Oligo-Mouse-Microbiota (OMM[12]) synthetic bacterial community[22], *Limosilactobacillus reuteri* I49 (DSM 32035) or *Bacteroides caecimuris* I48 (DSM 26085) alone or in combination with *Akkermansia mucinicphila* YL44 (DSM 26127). After the 2nd gavage, induction of postnatal genomic recombination was performed as described before. For preparation of the gavages, each bacteria was grown in Hungate tubes in Akkermansia medium[23] (AAM) for 24-48h under anaerobic conditions. Bacterial growth was assessed using OD600, adjusted to mix the same amount of each bacteria needed with a density of at least $3x10^7$ bacteria/ml, and glycerol was added (20% v/v final concentration). The gavages were sealed with a rubber septum in N_2 gased tubes and stored at -80°C until their transfer to the gnotobiotic facility.

Tissue processing and histopathological analysis. Small intestinal and colonic tissues were removed immediately after euthanization and dissected from adjacent tissue. The different parts of the gastrointestinal tract were cut open longitudinally, the content was removed, and the tissue processed as ‘swiss roles’. Tissues were fixed in 4% phosphate-buffered formalin for 48h, dehydrated, and embedded in melted paraffin (FFPE) or embedded in optical cutting temperature (OCT) medium without fixation. For histopathological assessment, 5µm sections were stained with hematoxylin (of Mayer) and 0.2% eosin (ethanolic solution; both Medite) in an automated staining machine (Leica). Ileal and colonic sections were blindly assessed for inflammation (tissue pathology index) based on infiltration of mononuclear cells into the individual wall layers (mucosa, submucosa and muscularis), hyperplasia and atypia of the crypts, depletion of goblet cells and epithelial damage, resulting in a score from 0 (non-inflamed) to 12 (severely inflamed). In addition, ileal and colonic sections were blindly assessed for an aberrant epithelial architecture via crypt architectural distortion (crypt hyperplasia, shifted nucleus-plasma relations, enlarged nuclei, nucleoli, apical shifted

mitoses) generating an aberrant epithelial index ranging from 0 (regular epithelium) to 4 (highly aberrant epithelium). Images were acquired by a PreciPoint M8 microscope (Precipoint).

Alcian blue / Periodicacid-Schiff (PAS-AB) staining. FFPE tissue sections (5µm) were stained with alcian blue (Fisher) for detection of acidic mucins (0.5% v/v in 3% acetic acid, pH=2.5, 5min) as well as periodic acid (0.5% v/v, 10min) co-stained with Schiff's reagent (Sigma-Aldrich) for neutral mucins (15min). Nuclei were counterstained with hematoxylin. Images were acquired by a PreciPoint M8 microscope (Precipoint).

Staining procedures. For immunohistochemical (IHC) and immunofluorescence (IF) stainings, FFPE tissue sections of intestinal swiss roles (5µM) were deparaffinized and rehydrated in an automated staining machine (Leica). After heat-mediated antigen retrieval with 10mM citrate buffer (pH=6; 23min; 900 watt), sections were incubated for 10min with 3% H_20_2 (Sigma-Aldrich) for IHC staining only. Subsequently, sections were blocked, and a primary antibody was applied overnight at 4°C. Buffer, solutions, antibodies, and dilutions are given in supplementary tables 1 and 2. After several washing steps, sections were incubated with the secondary antibody (fluorochrome or horseradish peroxidase coupled). In IF staining, 4′,6-diamidino-2-phenylindole (DAPI; 1:1000; Sigma-Aldrich) was used for nuclei staining and added to the secondary antibody solution. IF stainings were visualized using the Flouview FV10i microscope (Olympus). For IHC staining, antigen detection was performed by DAB/metal concentrate (Fisher), and nuclei were counterstained with hematoxylin. Stainings were scanned and further analyzed using a PreciPoint M8 microscope (Precipoint).

***In-situ* hybridization.** *In-situ* hybridization for murine *Lgr5* was performed on 5µm thick FFPE tissue sections using the RNAscope-2.5 HD *in-situ* assay kit-Brown (ACD, BioTechne GmbH) according to the manufacturer's instructions. The probe used was RNAscope Probe-Mm-Lgr5 from ACD. Sections were counterstained with hematoxylin, dipped in 0.02% ammonium hydroxide solution, and mounted. Stained slides were scanned and further analyzed via the PreciPoint M8 microscope (Precipoint).

Quantification of *Lgr5*-positive cells. *Lgr5*+ transcripts were quantified based on *Lgr5 in-situ* hybridization staining of colonic tissue sections. To determine *Lgr5*+ crypts, fifty well-oriented crypts were categorized as positive or negative for *Lgr5* expression. Crypts with at least one *Lgr5* transcript (each dot represents one transcript) counted as positive. The number of *Lgr5*+ crypts was calculated as a percentage of all crypts.

Quantification of Hsp60 expression. Hsp60 protein expression was quantified in Hsp60 IHC stainings of colonic tissue sections. To determine Hsp60+ crypts, fifty well-oriented crypts were categorized as positive, half-positive, or negative for Hsp60 expression. Half-positive crypts were crypts with a positive signal in only the left or right side of the crypt.

Quantification of goblet cells. The number of goblet cells was counted based on Alcian blue/Periodicacid-Schiff (PAS-AB) staining. Fifty well-oriented crypts were selected, and PAS+ cells were counted. The number of PAS+ cells was calculated as a total number per 100µm^2.

Quantification of crypt depth. Crypt depth was analyzed in H&E stainings of colonic tissue sections. In fifty well-oriented crypts, the length from the crypt base to crypt top was measured using the ViewPoint Light software, and the average length was calculated for each section.

mRNA isolation and quantitative real-time PCR. mRNA of total colonic tissue or small intestinal organoids was isolated using the NucleoSpin RNAII kit (Macherey-Nagel) according to the manufacturer's instructions. Quantitative Real-time PCR (qRT–PCR) was performed in duplicates using 1µl cDNA on a Light Cycler 480 system (Roche Diagnostics), applying the Universal Probe Library system according to the manufacturer's instructions. Primer sequences and probes are provided in supplementary table 3. Relative induction of gene mRNA expression was calculated by the $2^{-\Delta\Delta Ct}$ method using the expression of the housekeeper *Hprt* for normalization.

Quantitative qPCR of bacterial 16S rRNA genes. Quantitative PCR of the twelve different bacteria from the OMM[12] consortium was performed using 10ng gDNA as a template. Strain-specific 16S rRNA primers and hydrolysis probes were used for amplification[23]. For duplex qPCR assays, hydrolysis probes were 5′-labelled with either 6-carboxyfluorescein (FAM) or 6-carboxyhexafluorescein (HEX). qPCR standard curves were determined using linearized plasmids as DNA templates and run on a Light Cycler 480 system (Roche Diagnostics) in duplicates. A standard curve was then used for absolute quantification of 16S rRNA gene copy numbers of individual strains.

NanoString® analysis. Multiplexed gene expression of a panel of 768 metabolic genes was analyzed using the nCounter® Metabolic Pathway Panel (NanoString Technologies, Inc.) according to the manufacturer's instructions. In brief, 125ng isolated RNA of total colonic tissue underwent code set hybridization and was processed using a nCounter® MAX/FLEX system (NanoString Technologies, Inc.). Raw data were subjected to quality control, followed by normalization and analysis applying the nSolver Analysis Software (NanoString Technologies, Inc.).

RNA Microarray analysis. Total RNA was prepared from isolated colonic epithelial cells of Hsp60$^{\Delta/\Delta IEC}$ and Hsp60$^{fl/fl}$ mice on day 2 with the column-based NucleoSpin RNAII kit (Macherey-Nagel) according to the manufacturer's instructions. RNA concentration and quality were determined by spectrophotometric analysis (ND-1000, PEQLAB). RNA integrity number (RIN) was >8 for all samples (Agilent 1200 bioanalyzer, Alpha Metrix Biotech). Labeling of total RNA (100 ng) was performed with the Ambion WT Expression kit (Life Technologies), and

samples were hybridized to Affymetrix GeneChip Mouse Gene 1.1 ST arrays (Affymetrix) and scanned on an Affymetrix GeneTitan instrument. Probe sets were defined according to Dai *et al.*[46]. Probes were annotated and assigned to unique gene identifiers (Entrez IDs). The probes present on the Mouse Gene 1.1 ST arrays represent 21,225 Entrez IDs. Arrays were normalized with the Robust Multi-array Average (RMA) method. Only probe sets with normalized signal intensities above 20 on at least five arrays, interquartile range > 0.2, and at least 5 probes per probeset were selected for further analysis.

Mouse ELISA SAA. Saa concentration in murine plasma was quantified using a commercially available ELISA kit (ICL Inc.; Cat. num. E-90SAA) according to the manufacturer's instructions.

ChipCytometry. Cryo-preserved sections (7µm) were placed on a coverslip (Zellkraftwerk Chip Kit). Samples were fixed and transferred to the chip according to the manufacturer's instructions (Zellkraftwerk). The sections were scanned, and each position was photo-bleached for 20s using the ChipCytometry microscope (Zeiss). All photo-bleaching steps were performed with the built-in HBO lamp (Zeiss HBO 100 Microscope Illuminator with a 364nm long pass filter to protect epitope damage from UV light). Next, a background image was acquired in all channels using the ChipCytometry microscope. For the staining, 300µl antibody master mix was prepared. Details about the antibodies used are described in supplementary table 4. After acquisition of the background image, the chip was removed from the microscope, the antibody master mix was applied, and incubated in the dark for 30min. After several washing steps, the staining was scanned using the ChipCytometry microscope. For the next panel of antibodies, each position was again photo-bleached for 20s, and the background was re-adjusted. After the completion of all antibody panels, images were adjusted by finding the ideal combination between the contrast and the background in the ZellExplorer App of the ChipCytometry instrument. Signal intensity was analyzed using the Image J Fiji (https://imagej.net/software/fiji/) script from the GitHub repository (https://github.com/SebastianJarosch/ChipCytometry-Image-Processing). The intensity data obtained from Image J was converted to the FCS file format for quantitative analysis using writeFCS in MATLAB (https://de.mathworks.com/matlabcentral/fileexchange/42603-writefcs-fname-data-text-other) or fcswrite in python (https://github.com/ZELLMECHANIK-DRESDEN/fcswrite). The quantification was performed by gating the cell populations using the flow cytometry software (FlowJo).

Metagenomic DNA extraction from fecal samples. DNA was extracted from frozen mouse colonic content by bead-beating followed by a modified version of the protocol by Godon, as previously described[10]. Briefly, a volume of 600µL DNA stabilizing solution (Stratec Biomedical) was added to the fecal aliquots in 2ml screw-cap polypropylene microcentrifuge tubes containing 500mg sterile Silica beads (0.1-mm-diameter; BioSpec Products) on ice. After

the addition of 250µl of 4M guanidine thiocyanate – 0.1M Tris (pH=7.5) and 500µl of 5% *N*-lauroyl sarcosine – 0.1M phosphate buffer (pH=8.0), fecal suspensions were vortexed and incubated at 70°C for 1h with constant shaking. The mixture was mechanically disrupted by bead beating using a FastPrep®-24 bead beater (MP Biomedicals) supplied with a 24 × 2ml cooling adapter three times each for 40s at a speed of 6.5m/s. 15mg polyvinylpolypyrrolidone (PVPP, Sigma-Aldrich) was added as polyphenol adsorbent, and the suspension was centrifuged for 3min at 15,000×*g* at 4 °C. The supernatant was recovered and centrifuged for 3min at 15,000×*g* at 4°C. To remove bacterial RNA, a volume of 2µl RNAse (10mg/ml) was added to 500 µl clear supernatant and incubated at 37°C for 30min with constant shaking. Finally, the genomic DNA was purified using the NucleoSpin® gDNA clean-up kit (Macherey Nagel) following the manufacturer's instructions. The concentration and purity of the extracted DNA were determined using the NanoDrop® Spectrophotometer ND-1000 (ThermoFisher Scientific).

16S rRNA gene amplicon sequencing. After genomic DNA extraction, amplicon libraries (V3/V4 region) were amplified by PCR (25 cycles), purified using the AMPure XP system (Beckmann), pooled in an equimolar amount, and sequenced in paired-end mode (PE275) using a MiSeq system (Illumina, Inc.) according to the manufacturer's instructions and 25% (v/v) PhiX standard library. Raw sequences were processed using IMNGS based on the UPARSE approach[47]. Sequences were demultiplexed, trimmed to the first base with a quality score <3 and then paired. Sequences with less than 300 and more than 600 nucleotides and paired reads with an expected error >3 were excluded from the analysis. The remaining reads were trimmed by 5 nucleotides on each end to avoid GC bias and nonrandom base composition. The presence of chimeras was tested using UCHIME[48]. Clustering of zero-radius operational taxonomic units (zOTUs) was done at 97% sequence similarity. Taxonomic binning was assigned at an 80% confidence level using the RDP classifier[49] and compared to the SILVA ribosomal RNA gene database project[50]. Analysis was performed using the R-package Rhea[51]. In brief, rarefaction curves were used to assess sequencing depth and eliminate low-quality reads. zOTU counts were normalized, and percentage relative abundance was computed. Beta-diversity analysis was used to determine the diversity between groups based on generalized UniFrac distances. Alpha diversity within species was calculated based on species richness and Shannon effective number of species. EvolView was used to visualize phylogenetic trees[52].

Shallow shotgun metagenomics. Shallow shotgun metagenomic sequencing was performed on a NovaSeq machine (1G raw data with paired-end 150bp) using gDNA isolated from murine colonic content. After demultiplexing the data, adapters were trimmed from the raw sequencing reads using Trim Galore (https://github.com/FelixKrueger/TrimGalore). Reads were

subsequently processed with the KneadData quality control pipeline to remove low-quality read bases and murine contamination (https://bitbucket.org/biobakery/kneaddata/wiki/Home). Taxonomic profiling was performed using the MetaPhlAn3.0.13 classifier[53], which unambiguously classifies metagenomic reads to taxonomies based on a database of clade-specific marker genes derived from 17,000 microbial genomes (~13,500 bacterial and archaeal, ~3,500 viral, and ~110 eukaryotic). Species-level assignments were extracted, and data was centered log ratio scaled.

Generation of murine cecal water. To generate murine cecal water, approximately 150mg frozen cecal content was mixed with 3 sterile glass beads (2mm diameter; Glasschrott) and sterile PBS (10% w/v), followed by vigorous vortexing for 1min. To remove food debris, the samples were centrifuged (5min, 500g, 4°C), followed by the transfer of the supernatant into new tubes. After a second centrifugation step (5min, 8000g, 4°C), bacteria were pelleted, and the supernatant was distinguished as gut cecal water.

Primary crypt isolation and intestinal organoid culture. Primary small intestinal crypts from mice were isolated, and intestinal tissue (6-10cm) was inverted, digested with EDTA (30min; 4°C), and mechanically dissociated. The supernatant was filtered via a 70µm cell strainer, pelleted by centrifugation, and embedded in Matrigel (BD Biosciences). 25µl Matrigel®-organoid suspension was plated in 48 well plates (Eppendorf) and incubated in IntestiCult™ Organoid Growth Medium (STEMCELL Technologies) in a humidified 5% CO_2 atmosphere at 37°C. For subsequent passaging every 7-10 days, organoids were mechanically disrupted using a 1ml syringe with a 20G needle, pelleted by centrifugation, and embedded in fresh Matrigel. During experimental procedures, organoids were passaged three days before the start of the experiment and cultivated on self-made crypt culture medium (CCM). CCM contains advanced DMEM/F12 medium (Gibbco), 2mM GlutaMax (Gibbco), 10mM HEPES, penicillin, streptomycin and amphotericin (all Sigma-Aldrich) supplemented with N2, B27 (both Gibbco), 1mM N-acetylcysteine (Sigma-Aldrich), 50ng/ml EGF (ImmunoTools), 100ng/ml noggin and 0.5µg/ml R-spondin 1 (both PeproTec). Organoid pictures and videos for respective quantifications were generated using an Olympus CK X 41 microscope and Olympus cellSens Entry software.

Induction of *ex vivo* recombination and stimulation of organoids. *Ex vivo* induction of the *Hsp60* deletion in IECs was achieved by adding 500nM (Z)-4-hydroxytamoxifen (4-OHT; LKT) to the culture medium. After 24h, organoid culture media was changed to fresh CCM. Five days after *ex vivo Hsp60* deletion, organoids were treated for 24h with Tnf (50ng/µl; PeproTech Inc.), Ifnγ (1ng/µl; PeproTech Inc.), lipopolysaccharides (LPS; 1µg/ml; Sigma-Aldrich) or murine cecal water (dilution 1:500) and subsequently harvested for RNA isolation. For further Ido1 analysis, organoids were treated four days after *ex vivo Hsp60* deletion with the Ido1

agonist 3-hydroxyanthranilic acid (3-HAA; 200µM; Sigma-Aldrich) or the Ido1 antagonist dimethyltryptamine (1-D-MT; 1mM, Sigma-Aldrich) for 48h and were subsequently harvested for RNA isolation.

Organoid survival assay. To assess organoid survival, total numbers of propagating organoids were counted on day 1 after seeding (baseline), and numbers of viable organoids were subsequently determined at the indicated time points in the same well. Data are presented as a proportion of living organoids over baseline counts. Crypts were treated from seeding on with 3-hydroxyanthranilic acid (3-HAA; 200µM; Sigma-Aldrich).

Measurement of living cells and cellular ATP content. Live- and dead-cell protease activity was measured using the MultiTox-Fluor Cytotoxicity Assay, and ATP content was measured using the CellTiter-Glo Luminescent Cell Viability Assay (both from Promega), according to the manufacturer's instructions in a 48-well format. Fluorescence and luminescence were measured using the Tecan infinite M200 (Tecan Group Ltd.) and the i-control™ Microplate Reader software (Tecan).

Statistical analysis. Statistical analysis was performed with GraphPad Prism (version 8.0). Statistical tests used were: unpaired two-tailed *t*-test, analysis of variance (ANOVA) followed by pairwise comparison testing (Tukey), or by Kruskal-Wallis test followed by Dunn`s multiple comparison. $P < 0.05$ was considered significant. $^{*}P < 0.05$; $^{**}P < 0.01$; $^{***}P < 0.001$; $^{****}P < 0.0001$. Data are presented as mean ± sd, or in the case of weight curves, as mean ± sem.

Data availability. The demultiplexed reads for all 16S amplicon sequencing datasets from patient cohorts included in this manuscript are either publicly available or can be made available upon request. Raw data from HSCT and Enable cohorts have been deposited to the NCBI Sequence Read Archive [http://www.ncbi.nlm.nih.gov/sra] under the accession No. PRJNA565903 and No. PRJNA701859, respectively. Data from the UC cohort have been deposited to EMBL-EBI BioStudies database under the accession No. S-EPMC7599849. Software used to analyze the data are either freely or commercially available. Source code data are available from the corresponding author on request.

Supplementary table 1: Buffers and solutions used for IHC / IF staining.

Buffers and Solutions	Preparation
10mM Citrate buffer	2.94g sodium citrate tribasic dehydrate (Sigma- Aldrich) dH_2O up to 1l pH = 6
Phosphate buffered saline (10x)	20 tablets of PBS (Life Technologies) dH_2O up to 1l
Blocking buffer	2.5ml 10x PBS 1.25ml serum of the same species as the secondary antibody 21.25ml dH_2O 75µl Triton X-100 (100%; Sigma- Aldrich)
Antibody dilution buffer	4ml 10x PBS 36ml dH_2O 0.4g BSA (Sigma- Aldrich) 120µl Triton X-100 (100%; Sigma- Aldrich)

Supplementary table 2: Primary and secondary antibodies used for IHC / IF staining.

Primary antibody	Species	Manufacturer	Dilution	Cat. #
Anti-Hsp60 (IF)	goat	Enzo	1:150	ADI-SPA-828-F
Anti-Hsp60 (IHC)	rabbit	Cell Signaling Technology	1:400	12165
Anti-Ido1	rat	Enzo	1:200	ALX-804-901-0100
Anti-Ki67	rabbit	Cell Signaling Technology	1:300	12202
Secondary antibody	**Species**	**Manufacturer**	**Dilution**	
Alexa Fluor anti-goat 488	donkey	Life Technologies	1:200	
Alexa Fluor anti-rat 594	donkey	Life Technologies	1:200	
Alexa Fluor anti-rabbit 647	donkey	Life Technologies	1:200	
Anti-rabbit HRP	donkey	Dianova	1:300	

Supplementary table 3: Primer sequences and UPL probe numbers used for qRT-PCR analysis.

Target gene	Forward primer (L)	Reverse primer (R)	UPL probe #
Hprt	TCCTCCTCAGACCGCTTTT	CCTGGTTCATCATCGCTAATC	95
Hsp60/Hspd1	TCTTCAGGTTGTGGCAGTCA	CCCCTCTTCTCCAAACACTG	1
Tnf	TGCCTATGTCTCAGCCTCTTC	GAGGCCATTTGGGAACTTCT	49
Trb3	GTCGCTTTGTCTTCAGCAACT	TCATCTGATCCAGTCATCACG	67

Supplementary table 4: Antibodies used for cryo-preserved tissue stainings with ChipCytometry.

Antibody	Fluorophore	Concentration	Company	Cat #
CD3	PE	1:200	BioLegend	100308
CD4	PecP/Cy5.5	1:100	BioLegend	300529
CD8α	PecP/Cy5.5	1:50	BioLegend	100734
CD11b	PecP/Cy5.5	1:50	BioLegend	101227
CD11c	FITC	1:100	Life Technologies	11-0114-81
CD19	FITC	1:100	BD	553785
FoxP3	efluor570	1:50	Thermo Fisher Scientific	47-5773-80
Hoechst	BUV395	1:100000	Thermo Fisher Scientific	H3570
IgA	AF647	1:50	SouthernBiotech	743293
Ly6G	PE	1:100	BD	553128
NK1.1	AF488	1:200	BioLegend	108718
Pan-cytokeratin	AF488	1:500	BioLegend	628608

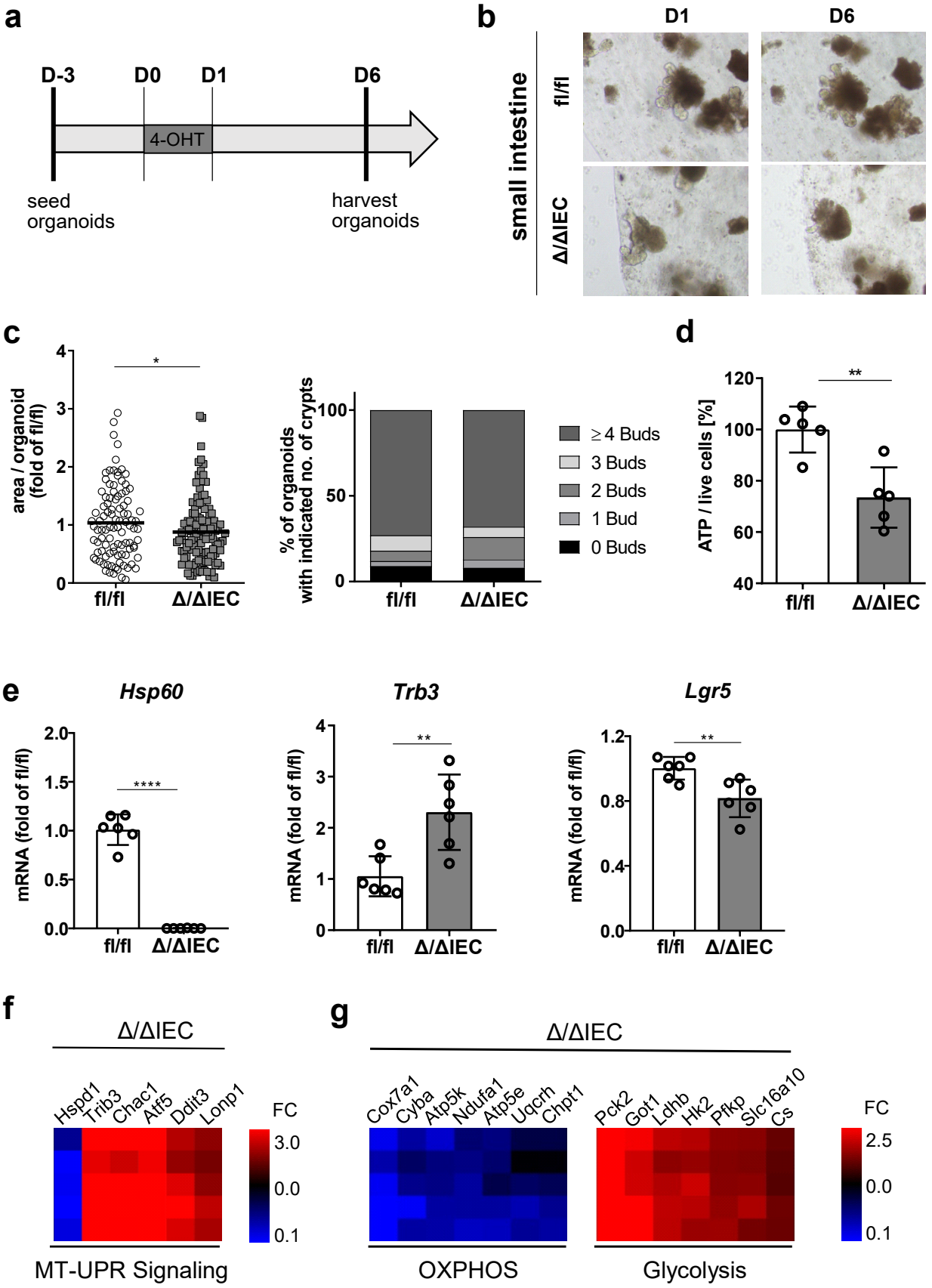

Extended Data Figure 1

Extended Data Fig.1: Mitochondrial dysfunction impacts stemness and cellular metabolism.

a, Experimental setup. Small intestinal crypts were isolated and seeded in Matrigel®, followed by Hsp60 deletion *ex vivo* via tamoxifen addition to the media. Organoids were analyzed 6 days after *ex vivo* Hsp60 deletion. **b,** Representative pictures of organoids with a Hsp60 deficiency (Δ/ΔIEC; Ctrl: fl/fl). **c,** Quantification of organoid area and *de novo* crypt formation (number of buds) at day 6 in the respective genotypes. **d,** ATP measured per live cells at day 6 in the respective genotypes. **e,** qPCR of the mitochondrial chaperone *Hsp60*, the MT-UPR marker gene *Trb3* and the stem cell marker *Lgr5*. **f, g,** Colonic crypts of $Hsp60^{\Delta/\Delta IEC}$ and $Hsp60^{fl/fl}$ mice were isolated at day 2, and RNA microarray analysis of genes related to (**f**) MT-UPR signaling or **(g)** OXPHOS and glycolysis was performed (data presented as fold change of $Hsp60^{\Delta/\Delta IEC}$ over $Hsp60^{fl/fl}$).

Data are represented by mean ± s.d. of (**c**) 100 organoids, (**d**) five or (**e**) six technical replicates. (**f,g**) Data include four biological replicates. P-values were calculated by ANOVA followed by pairwise comparison testing (Tukey). *P<0.05, **P<0.01, ***P<0.001, ****P<0.0001.

D: day; Hsp60: heat shock protein 60; 4-OHT: tamoxifen; IECs: intestinal epithelial cells; MT-UPR: mitochondrial unfolded protein response; Trb3: tribbles pseudokinase 3; Lgr5: leucine-rich repeat-containing G-protein coupled receptor 5¸ OXPHOS: oxidative phosphorylation.

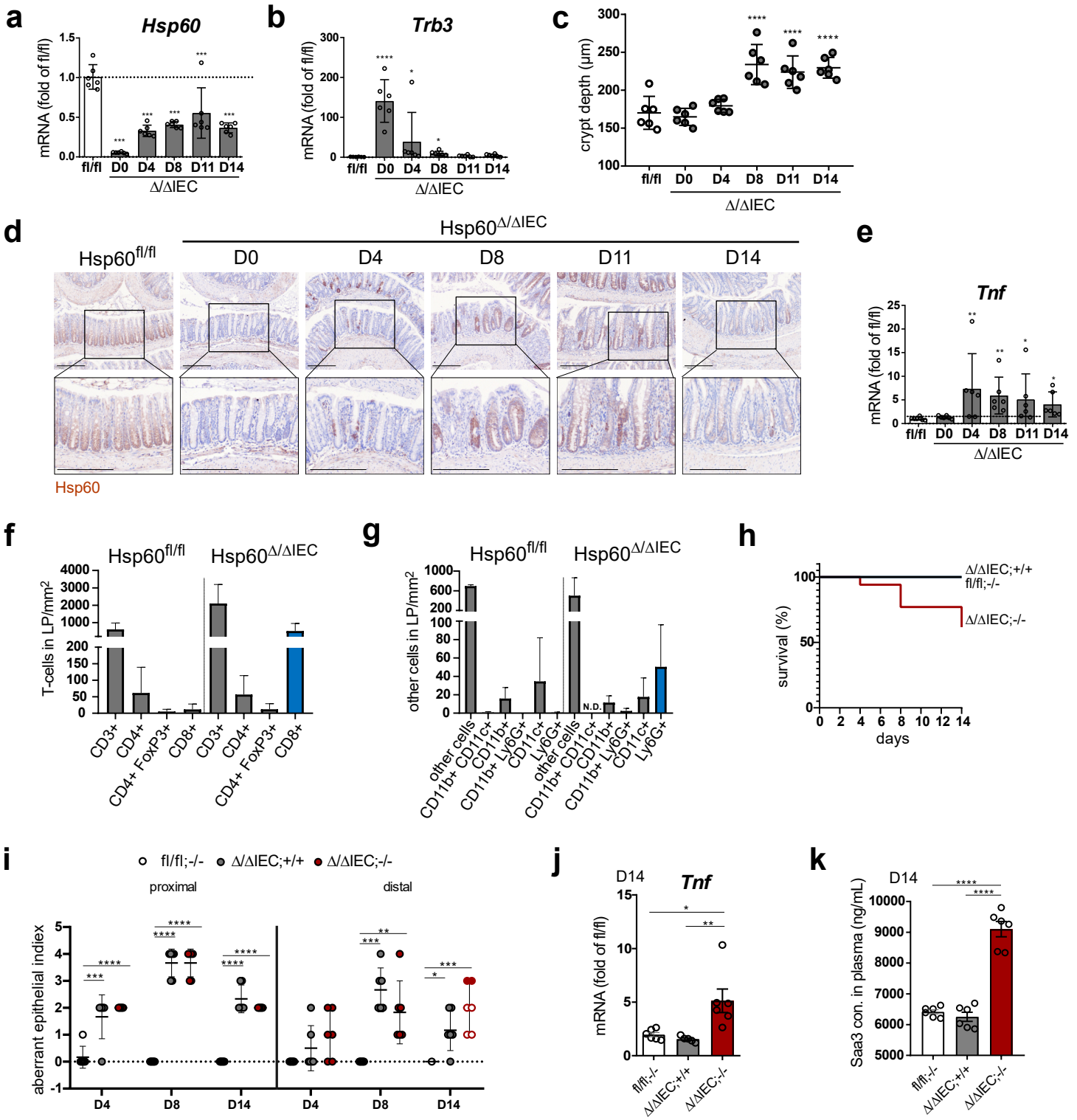

Extended Data Figure 2

Extended Data Fig.2: Metabolic injury accelerates the onset of inflammation.

a, b, qPCR of (**a**) the mitochondrial chaperone *Hsp60* and (**b**) the MT-UPR marker gene *Trb3* using mRNA of whole colonic tissue from days 0 to 14 in Hsp60$^{\Delta/\Delta IEC}$ and Hsp60$^{fl/fl}$ mice. **c,** Crypt depth of H&E stainings of colonic tissue of Hsp60$^{\Delta/\Delta IEC}$ and Hsp60$^{fl/fl}$ mice was measured from days 0 to 14. **d,** Representative images of immunohistochemistry staining of Hsp60 in colonic tissue of Hsp60$^{\Delta/\Delta IEC}$ and Hsp60$^{fl/fl}$ mice from days 0 to 14. Brown color shows specific Hsp60 signal, nuclei are stained with hematoxylin. Scale bars: 200µm. **e,** qPCR of the pro-inflammatory cytokine *Tnf* using mRNA of whole colonic tissue from days 0 to 14 in Hsp60$^{\Delta/\Delta IEC}$ and Hsp60$^{fl/fl}$ mice. **f,** Quantification of the different T-cell populations in the colonic LP per mm^2 in Hsp60$^{\Delta/\Delta IEC}$ and Hsp60$^{fl/fl}$ mice at day 8 from a ChipCytometry staining. T-cells are stained as follows: CD3 (red), CD4 (green), CD8a (blue), Foxp3 (cyan). Nuclei are stained using Hoechst (grey), and epithelial cells using Pan-cytokeratin (yellow). **g,** Quantification of the different innate immune cell populations in the colonic LP per mm^2 in Hsp60$^{\Delta/\Delta IEC}$ and Hsp60$^{fl/fl}$ mice at day 8 from a ChipCytometry staining. Immune cells are stained as follows: CD3 (red), CD11b (green), Ly6G (blue). Nuclei are stained using Hoechst (grey) and epithelial cells using Pan-cytokeratin (yellow). **h,** Survival (%) of Hsp60$^{\Delta/\Delta IEC}$;*Il10*$^{-/-}$ (Ctrl: Hsp60$^{\Delta/\Delta IEC}$;*Il10*$^{+/+}$, Hsp60$^{fl/fl}$;*Il10*$^{-/-}$) mice from days 0 to 14. **i,** H&E stainings of colonic tissue (proximal vs. distal) of Hsp60$^{\Delta/\Delta IEC}$;*Il10*$^{-/-}$ (Ctrl: Hsp60$^{\Delta/\Delta IEC}$;*Il10*$^{+/+}$, Hsp60$^{fl/fl}$;*Il10*$^{-/-}$) mice from days 4, 8, and 14 were histologically scored for an aberrant epithelium. The red filled circles represent the two Hsp60$^{\Delta/\Delta IEC}$;*Il10*$^{-/-}$ mice with accelerated inflammation. The red open circles represent the four Hsp60$^{\Delta/\Delta IEC}$;*Il10*$^{-/-}$ mice without accelerated inflammation. **j, k,** (**j**) qPCR of *Tnf* using mRNA of whole colonic tissue from day 14 and (**k**) ELISA of Saa using serum from day 14 of Hsp60$^{\Delta/\Delta IEC}$;*Il10*$^{-/-}$ (Ctrl: Hsp60$^{\Delta/\Delta IEC}$;*Il10*$^{+/+}$, Hsp60$^{fl/fl}$;*Il10*$^{-/-}$) mice.

Data are represented by mean ± s.d. of (**a,b,c,e,i,j,k**) six or **(f,g**) two biological replicates. (**a,b,c,e,i,j,k**) P-values were calculated by ANOVA followed by pairwise comparison testing (Tukey). *P<0.05, **P<0.01, ***P<0.001, ****P<0.0001.

D: day; Hsp60: heat shock protein 60; IECs: intestinal epithelial cells; MT-UPR: mitochondrial unfolded protein response; Trb3: tribbles pseudokinase 3; Tnf: tumor necrosis factor; LP: lamina propria; IL10: interleukin-10, Saa: serum amyloid A.

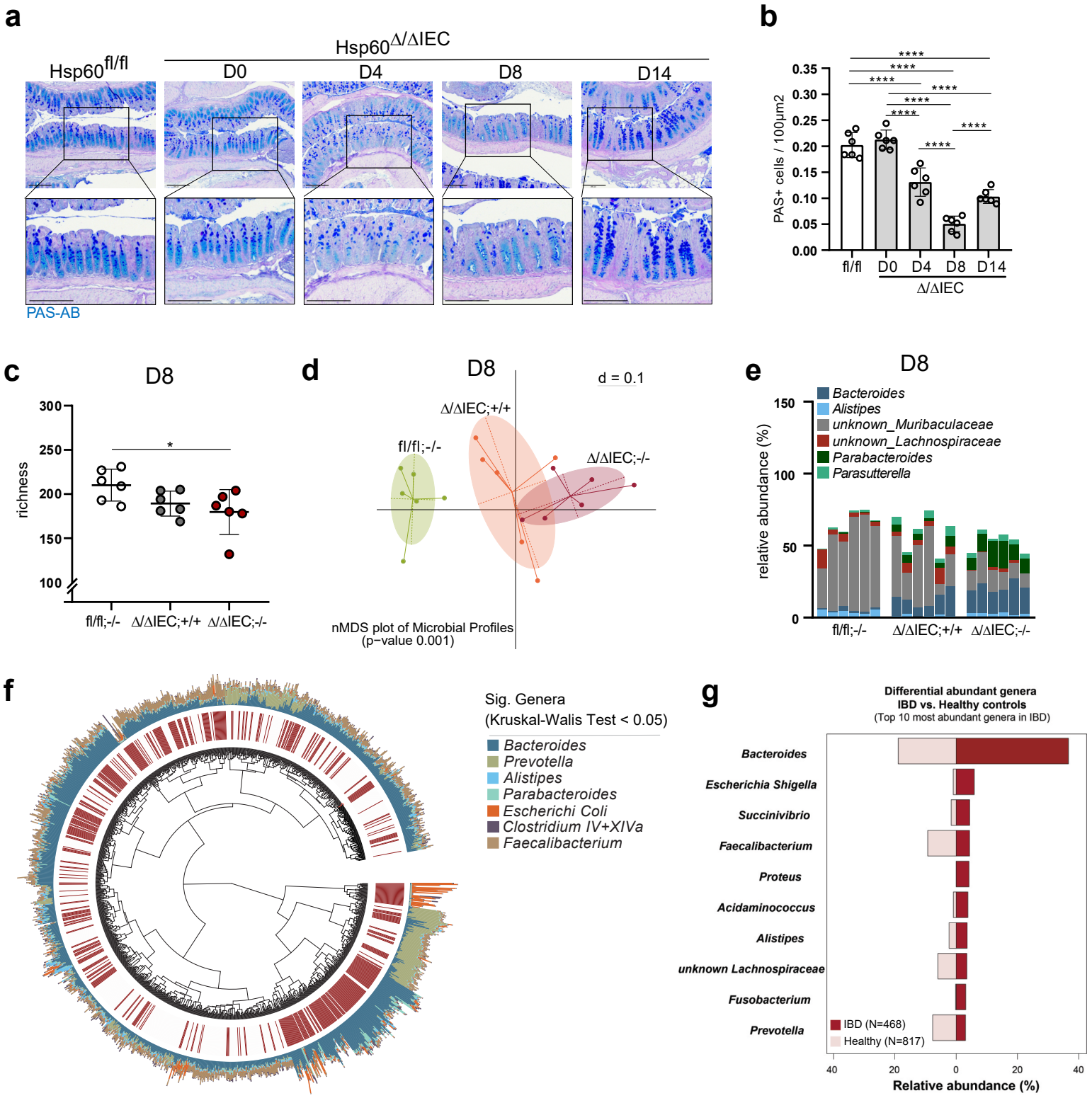

Extended Data Figure 3

Extended Data Fig.3: Metabolic injury drives dysbiotic changes in the intestinal microbiota.

a, Representative images of PAS-AB staining in colonic tissue of Hsp60$^{\Delta/\Delta IEC}$ and Hsp60$^{fl/fl}$ mice from days 0 to 14. Acidic mucins are stained in cyan, neutral mucins in dark blue. Nuclei are stained with hematoxylin. Scale bars: 200µm. **b,** Quantification of PAS positive cells per 100µm^2 in colonic tissue of Hsp60$^{\Delta/\Delta IEC}$ and Hsp60$^{fl/fl}$ from days 0 to 14. **c,** *Alpha*-diversity measured by species richness in feces of Hsp60$^{\Delta/\Delta IEC}$;*Il10*$^{-/-}$ (Ctrl: Hsp60$^{\Delta/\Delta IEC}$;*Il10*$^{+/+}$, Hsp60$^{fl/fl}$;*Il10*$^{-/-}$) mice at day 8. **d,** *Beta*-diversity depicted as nMDS plot of microbial profiles of fecal samples stratified by genotype (Hsp60$^{\Delta/\Delta IEC}$;*Il10*$^{-/-}$, Hsp60$^{\Delta/\Delta IEC}$;*Il10*$^{+/+}$ and Hsp60$^{fl/fl}$;*Il10*$^{-/-}$ mice) at day 8. **e,** Relative abundance of significantly enriched genera in Hsp60$^{\Delta/\Delta IEC}$;*Il10*$^{-/-}$ (Ctrl: Hsp60$^{\Delta/\Delta IEC}$;*Il10*$^{+/+}$, Hsp60$^{fl/fl}$;*Il10*$^{-/-}$) mice at day 8. **f,** Relative abundance of significantly enriched genera of the fecal microbiota in IBD patients (N=468) and healthy controls (N=817). The dendrogram depicts similarities between microbiota profiles based on generalized UniFrac distances between all 1285 individuals. Individual taxonomic composition at the genus level is shown as stacked bar plots around the dendrogram in addition to health status (red: IBD patients). **g,** Relative abundance of the top ten differential abundant genera in IBD patients (N=468) versus healthy controls (N=817).

(**b,c**) Data are represented by mean ± s.d. of six biological replicates. P-values were calculated by ANOVA followed by pairwise comparison testing (Tukey). *P<0.05, **P<0.01, ***P<0.001, ****P<0.0001. (**d,f**) Kruskal-Wallis test was used to select significant genera (P<0.05).

D: day; Hsp60: heat shock protein 60; IECs: intestinal epithelial cells; IL10: interleukin-10; PAS-AB: Alcian blue/Periodicacid-Schiff; IBD: inflammatory bowel diseases.

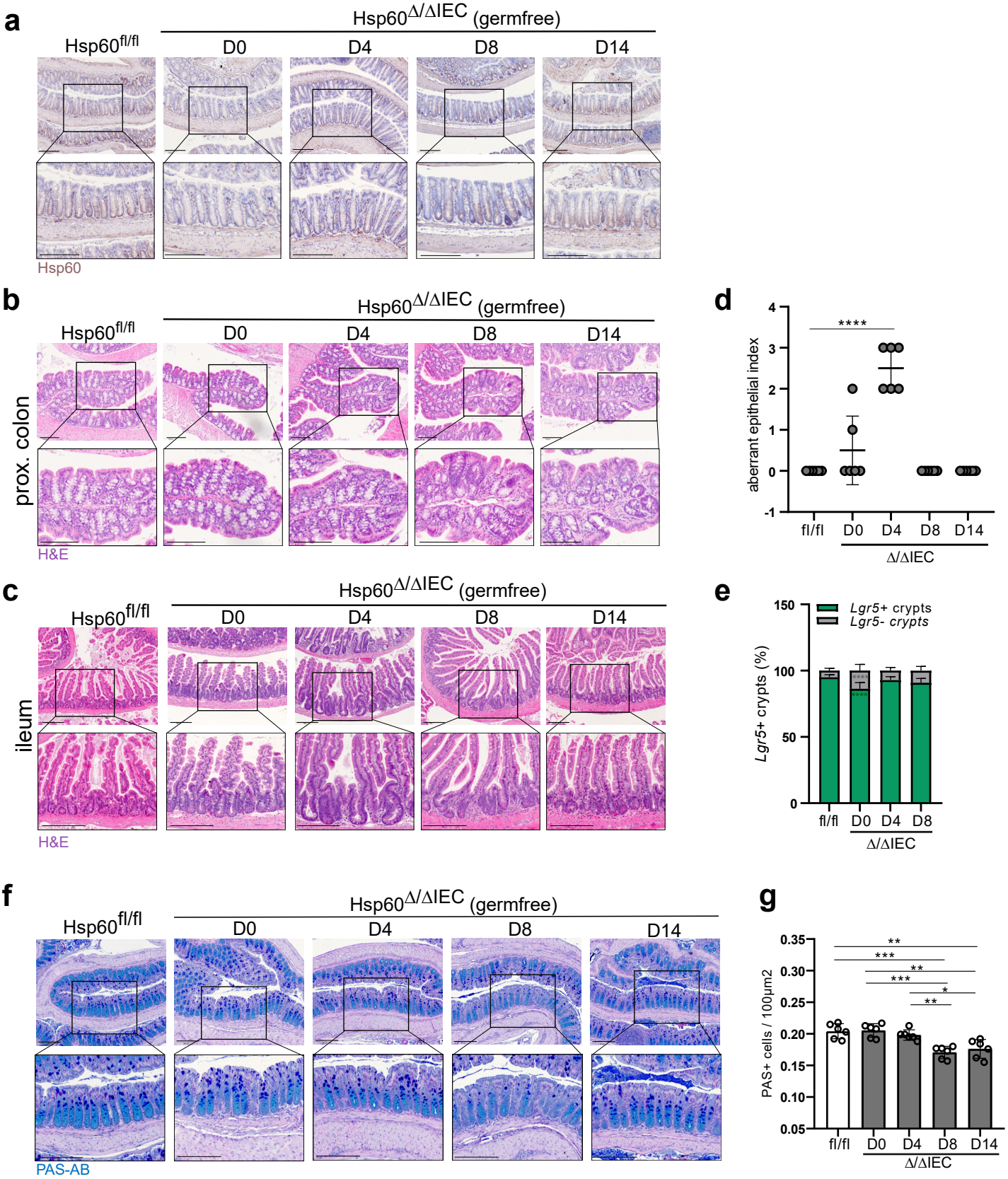

Extended Data Figure 4

Extended Data Fig.4: Bacterial control of metabolic injury.

a, Representative images of immunohistochemistry staining of Hsp60 in distal colonic tissue of GF Hsp60$^{\Delta/\Delta IEC}$ and Hsp60$^{fl/fl}$ mice from days 0 to14. Brown color shows specific Hsp60 signal, nuclei are stained with hematoxylin. Scale bars: 200µm. **b, c,** Representative images of H&E staining of (**b**) proximal colonic and (**c**) ileal tissue of GF Hsp60$^{\Delta/\Delta IEC}$ and Hsp60$^{fl/fl}$ mice from days 0 to 14. Scale bars: 200µm. **d,** H&E stainings of ileal tissue of GF Hsp60$^{\Delta/\Delta IEC}$ mice from days 0 to 14 were histologically scored for an aberrant epithelium. **e,** Quantification of *Lgr5*-negative and -positive crypts in GF Hsp60$^{\Delta/\Delta IEC}$ and Hsp60$^{fl/fl}$ mice from days 0 to 8 using *in-situ* hybridization of *Lgr5* in distal colonic swiss roles. **f,** Representative images of PAS-AB staining in distal colonic tissue of GF Hsp60$^{\Delta/\Delta IEC}$ and Hsp60$^{fl/fl}$ mice from days 0 to 14. Acidic mucins are stained in cyan, neutral mucins in dark blue. Nuclei are stained with hematoxylin. Scale bars: 200µm. **g,** Quantification of PAS positive cells per 100µm^2 in distal colonic tissue of GF Hsp60$^{\Delta/\Delta IEC}$ and Hsp60$^{fl/fl}$ from days 0 to 14.

(**d,e,g**) Data are represented by mean ± s.d. of six biological replicates. P-values were calculated by (**d,g**) One-way or (**e**) Two-way ANOVA followed by pairwise comparison testing (Tukey). *P<0.05, **P<0.01, ***P<0.001, ****P<0.0001.

D: day; GF: germfree; Hsp60: heat shock protein 60; IECs: intestinal epithelial cells; H&E: hematoxylin and eosin; Lgr5: Leucine-rich repeat-containing G-protein coupled receptor 5; PAS-AB: Alcian blue/Periodicacid-Schiff.

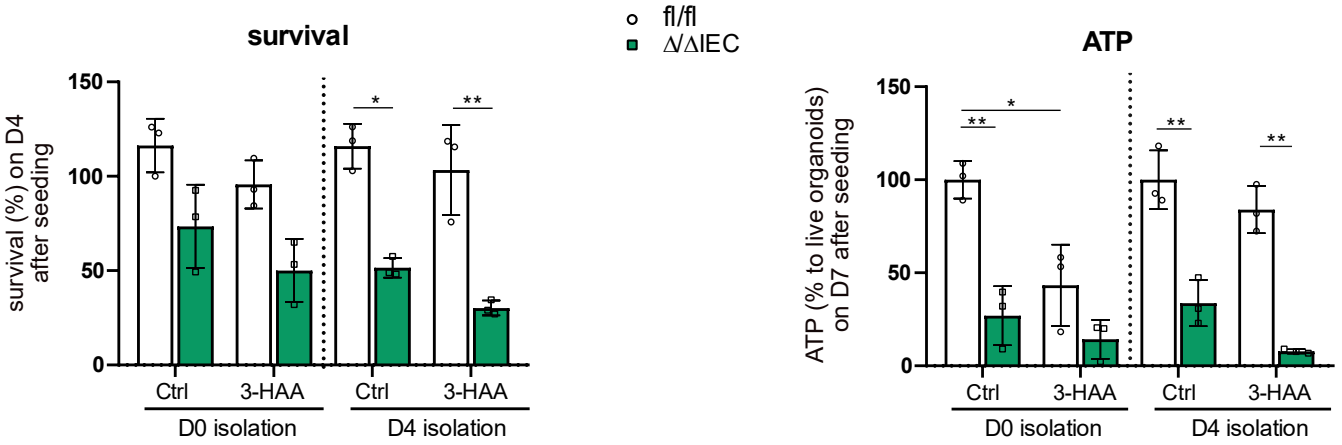

Extended Data Figure 5

Extended Data Fig.5: Host-tryptophan metabolism is rewired during metabolic injury.

a, Survival and ATP levels of colonic organoids isolated from murine crypts with an *in vivo* Hsp60 deletion ($Hsp60^{\Delta/\Delta IEC}$; Ctrl: $Hsp60^{fl/fl}$). Crypts were isolated at day 0 or 4 after complete Hsp60 deletion and immediately treated with 3-HAA..

Data are represented by mean ± s.d. of three biological replicates. P-values were calculated by ANOVA followed by pairwise comparison testing (Tukey). *P<0.05, **P<0.01, ***P<0.001, ****P<0.0001.

D: day; Hsp60: heat shock protein 60; IECs: intestinal epithelial cells; 3-HAA: 3-hydroxyanthranilic acid, ATP: adenosine triphosphate.

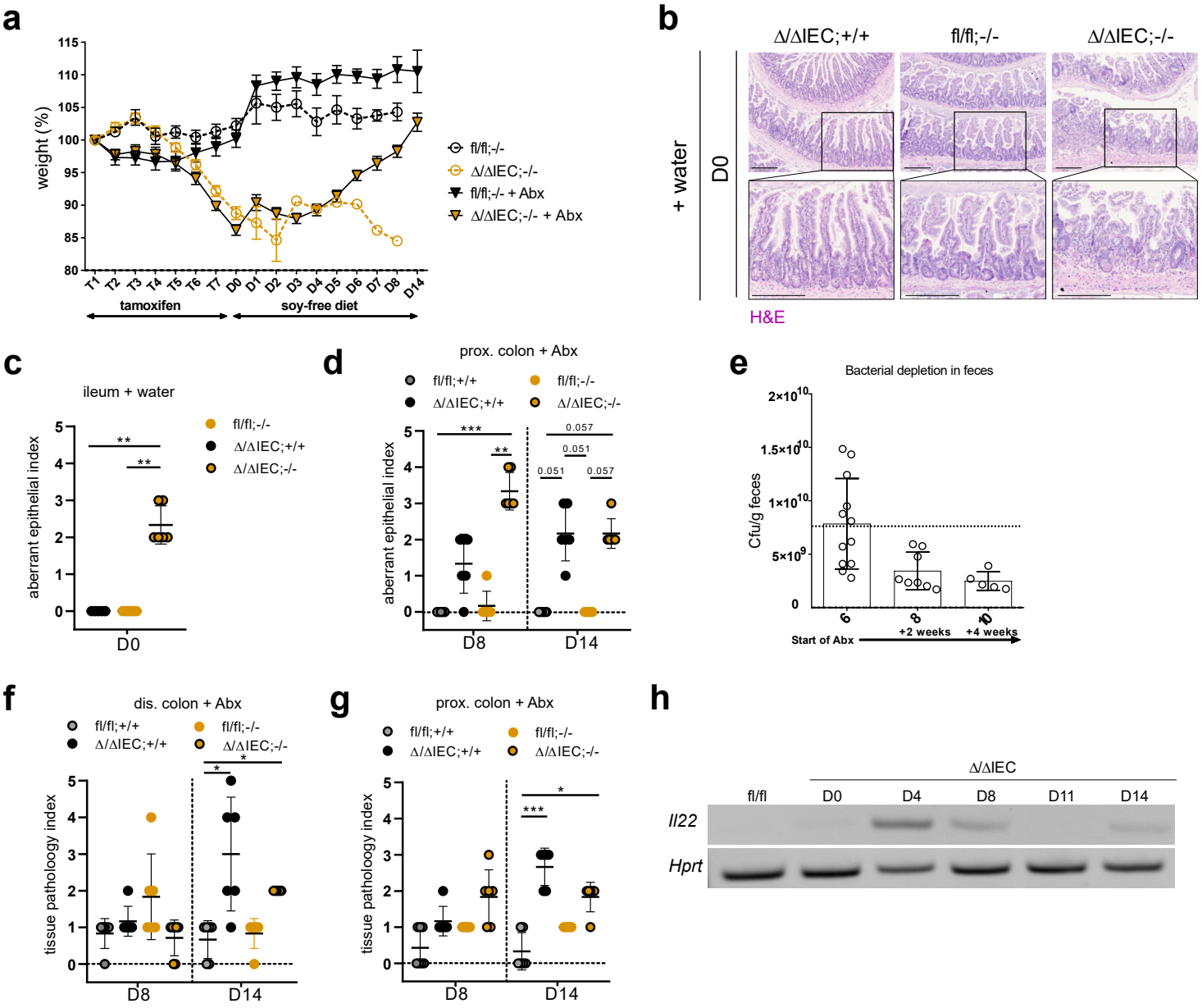

Extended Data Figure 6

Extended Data Fig.6: Ahr signaling is a protective mechanism against metabolic injury.

a, Relative weight curve of Hsp60$^{\Delta/\Delta IEC}$;*AhR*$^{-/-}$ mice treated with or without Abx (Ctrl: Hsp60$^{fl/fl}$;*AhR*$^{-/-}$) from the start of tamoxifen feeding until sampling time point. **b, c,** (**b**) Representative images of H&E staining and (**c**) histological scoring for an aberrant epithelium of ileal tissue of Hsp60$^{\Delta/\Delta IEC}$;*AhR*$^{-/-}$ (Ctrl: Hsp60$^{\Delta/\Delta IEC}$;*AhR*$^{+/+}$, Hsp60$^{fl/fl}$;*AhR*$^{-/-}$) mice at day 0 treated without Abx. Scale bars: 200µm. **d,** H&E stainings of proximal colonic tissue of Hsp60$^{\Delta/\Delta IEC}$;*AhR*$^{-/-}$ (Ctrl: Hsp60$^{\Delta/\Delta IEC}$;*AhR*$^{+/+}$, Hsp60$^{fl/fl}$;*AhR*$^{-/-}$) mice at days 8 and 14 treated with Abx were histologically scored for an aberrant epithelium. **e,** Quantification of CFUs per gram murine feces before and 2 and 4 weeks after starting treatment with Abx. Abx were started at the age of 6 weeks. **f, g,** H&E stainings of (**f**) distal and (**g**) proximal colonic tissue of Hsp60$^{\Delta/\Delta IEC}$;*AhR*$^{-/-}$ (Ctrl: Hsp60$^{\Delta/\Delta IEC}$;*AhR*$^{+/+}$, Hsp60$^{fl/fl}$;*AhR*$^{-/-}$) mice at days 8 and 14 treated with Abx were histologically scored for inflammation. **h,** Agarose gel of qPCR from *Il22* (and the housekeeper *Hprt*) using mRNA of whole colonic tissue from days 0 to 14 in Hsp60$^{\Delta/\Delta IEC}$ and Hsp60$^{fl/fl}$ mice. One gel line includes a mix of six biological replicates.

Data are represented by (**a**) mean ± sem or mean ± s.d. of (**c,d,f,g**) six or (**e**) six to twelve biological replicates. (**c**) P-values were calculated by ANOVA followed by pairwise comparison testing (Tukey). (**d,f,g**) P-values were calculated by Kruskal-Wallis followed by Dunn's post-test comparisons. *P<0.05, **P<0.01, ***P<0.001, ****P<0.0001.

Hsp60: heat shock protein 60; IECs: intestinal epithelial cells; AhR: aryl hydrocarbon receptor; Abx: antibiotics; H&E: hematoxylin and eosin; CFUs: colony forming units, IL-22: interleukin 22.

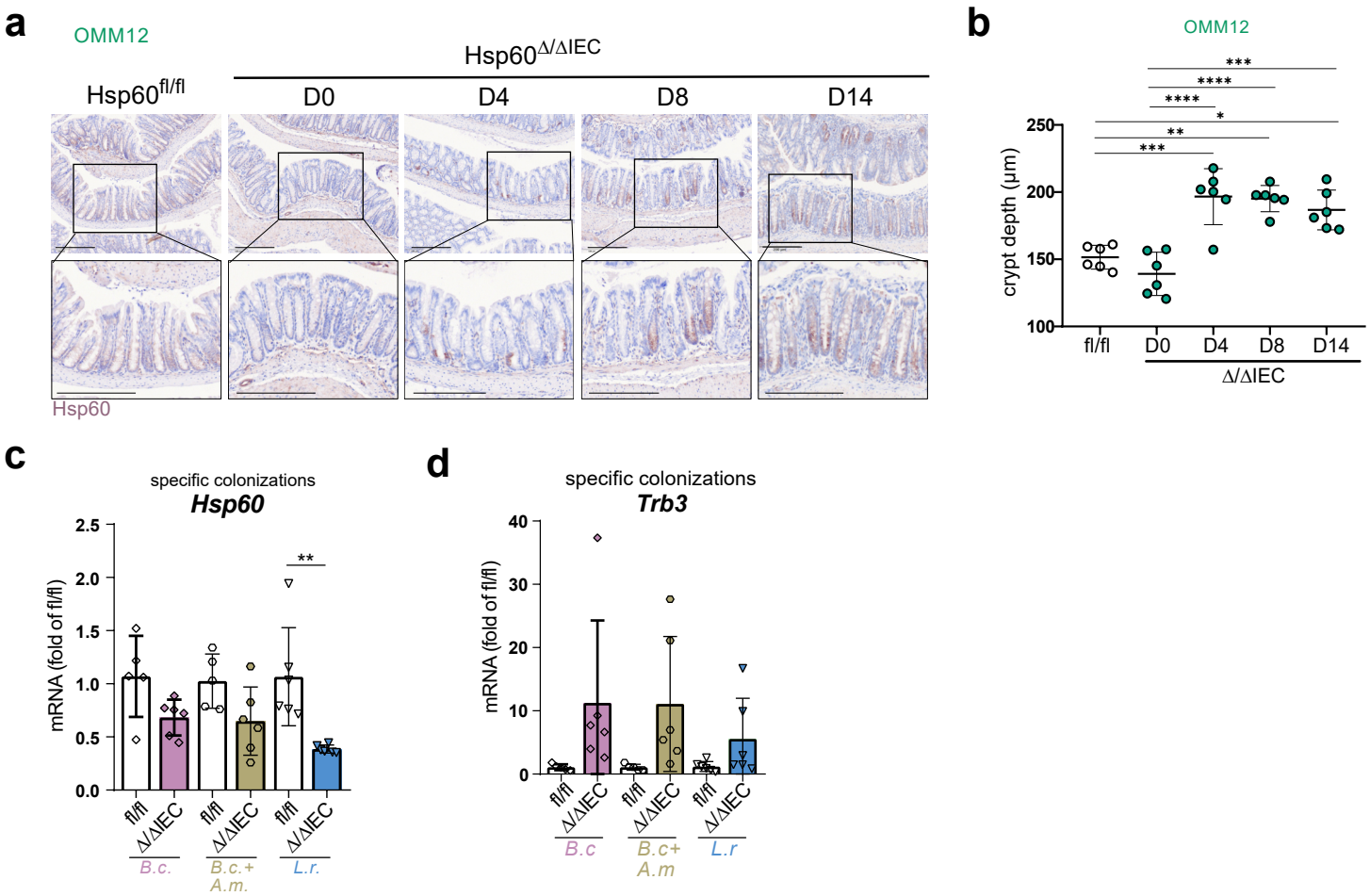

Extended Data Figure 7

Extended Data Fig.7: *B. caecimuris* induces metabolic injury.

a, Representative images of immunohistochemistry staining of Hsp60 of distal colonic tissue of GF Hsp60$^{\Delta/\Delta IEC}$ and Hsp60$^{fl/fl}$ mice colonized with the Oligo-Mouse-Microbiota (OMM^{12}) synthetic bacterial community from days 0 to 14 after Hsp60 deletion. Scale bars: 200µm. **b,** Crypt depth of H&E stainings of distal colonic tissue of GF Hsp60$^{\Delta/\Delta IEC}$ and Hsp60$^{fl/fl}$ mice colonized with OMM^{12} was measured from days 0 to 14. **c, d,** qPCR of (**c**) the mitochondrial chaperone *Hsp60* and (**d**) the MT-UPR marker gene *Trb3* using mRNA of whole colonic tissue of GF Hsp60$^{\Delta/\Delta IEC}$ and Hsp60$^{fl/fl}$ mice colonized with *Bacteroides caecimuris*, *Bacteroides caecimuris* and *Akkermanisa muciniphila* or *Limosilactobacillus reuteri* sampled on day 8.

(**b-d**) Data are represented by mean ± s.d. of six biological replicates. P-values were calculated by ANOVA followed by pairwise comparison testing (Tukey). *P<0.05, **P<0.01, ***P<0.001, ****P<0.0001.

GF: germfree; D: day; Hsp60: heat shock protein 60; IECs: intestinal epithelial cells; MT-UPR: mitochondrial unfolded protein response; Trb3: tribbles pseudokinase 3; H&E: hematoxylin and eosin.

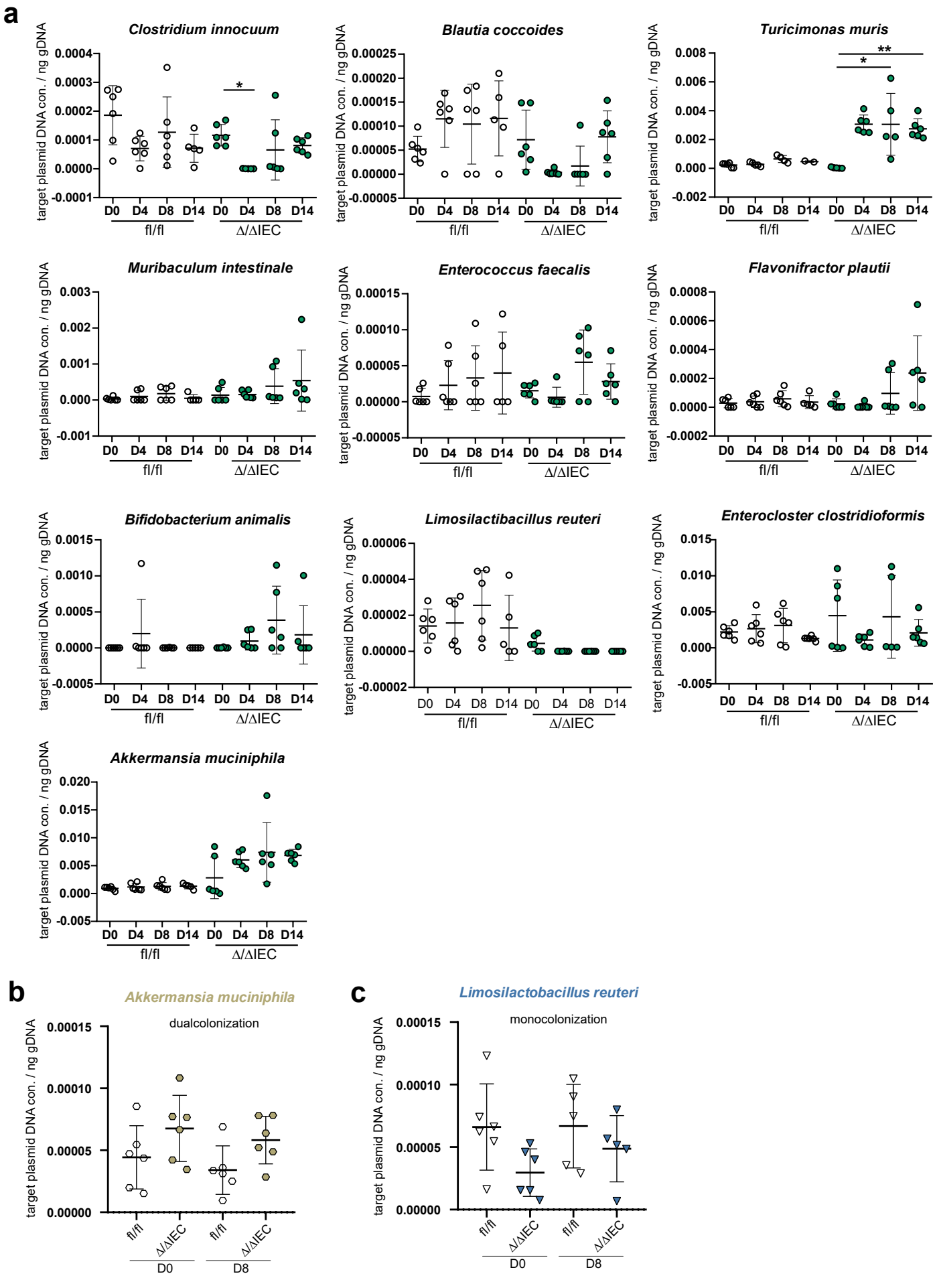

Extended Data Figure 8

Extended Data Fig.8: Relative abundance of bacteria in selective colonizations.

a, Abundance of 10 different species from the Oligo-Mouse-Microbiota (OMM^{12}) synthetic bacterial community in feces of GF $Hsp60^{\Delta/\Delta IEC}$ and $Hsp60^{fl/fl}$ mice colonized with OMM^{12} detected by 16S targeted qPCR from days 0 to 14. **b,** Abundance of *Akkermanisa muciniphila* in feces of GF $Hsp60^{\Delta/\Delta IEC}$ and $Hsp60^{fl/fl}$ mice dual-colonized with *Bacteroides caecimuris* and *Akkermanisa muciniphila* detected by 16S targeted qPCR at days 0 and 8. **c,** Relative abundance of *Limosilactobacillus reuteri* in feces of GF $Hsp60^{\Delta/\Delta IEC}$ and $Hsp60^{fl/fl}$ mice colonized with *Limosilactobacillus reuteri* detected by 16S targeted qPCR at days 0 and 8.

Data are represented by mean ± s.d. of six biological replicates. (**a**) P-values were calculated by Kruskal-Wallis test followed by Dunn's post-test for multiple comparisons. (**b,c**) P-values were calculated by ANOVA followed by pairwise comparison testing (Tukey). *P<0.05, **P<0.01, ***P<0.001, ****P<0.0001.

GF: germfree; D: day; Hsp60: heat shock protein 60; IECs: intestinal epithelial cells.